Original Article

A SMART POLYHYDROXYALKANOATE-HYALURONIC ACID HYBRID BIPHASIC DELIVERY PLATFORM FOR ENHANCED ALZHEIMER'S SYMPTOM MANAGEMENT VIA SUSTAINED HUPERZINE A RELEASE

Jianfei Wu[1,§], Yanwen Zhou[2,§], Yu Liu[1], Yu Yang[1], Yuandong Tang[3], Youguo Tan[1], Duanfang Cai[1], Kezhi Liu[1,4], and Daixu Wei[1,5,*]

[1]Zigong Institute of Brain Science, Zigong Psychiatric Research Center, Zigong Affiliated Hospital of Southwest Medical University, 643021 Zigong, Sichuan, China
[2]Faculty of Life Sciences and Medicine, Northwest University, 710069 Xi'an, Shaanxi, China
[3]Department of Special Examinations, Zigong Affiliated Hospital of Southwest Medical University, 643021 Zigong, Sichuan, China
[4]Department of Psychiatry, Affiliated Hospital of Southwest Medical University, 646000 Luzhou, Sichuan, China
[5]Clinical Medical College and Affiliated Hospital of Chengdu University, Chengdu University, 610106 Chengdu, Sichuan, China
[§]These authors contributed equally.

Abstract

Background: Huperzine A (HupA), a potent and selective acetylcholinesterase inhibitor with neuroprotective properties, faces significant clinical challenges in Alzheimer's disease (AD) management. Its amphiphilic nature results in poor encapsulation efficiency within conventional hydrophobic polyesters or hydrophilic hydrogels, while its requirement for repeated dosing leads to systemic toxicity and poor patient compliance. **Methods:** We developed a novel hyaluronic acid (HA)-based biphasic delivery platform. This system utilized a HA gel matrix to encapsulate HupA-loaded polyhydroxyalkanoate nanoparticles (HupA@(NP/Gel)). Its sustained-release efficacy and therapeutic efficacy were evaluated in AD mice through a single administration, followed by behavioral, biochemical, and histopathological analyses. **Results:** The HupA@(NP/Gel) platform achieved complete drug encapsulation and successfully extended HupA release for over 20 days, matching the therapeutic requirements for AD. This sustained delivery translated to therapeutic efficacy *in vivo*: it significantly ameliorated core AD pathologies, including reduced Aβ deposition and restored cholinergic function. Moreover, the treatment conferred comprehensive neuroprotection by suppressing glial activation and neuroinflammation, enhancing neuronal survival, and preserving synaptic integrity. Crucially, these multifaceted benefits resulted in improved spatial memory and reduced anxiety/depression-like behaviors. **Conclusions:** Our study demonstrates that the HupA@(NP/Gel) system can serve as an effective and translatable strategy for AD intervention. By effectively overcoming the key hurdles of HupA delivery, this work establishes a translatable sustained-delivery strategy that highlights carbohydrate polymer technology's role in neurologic therapeutics.

Keywords: Alzheimer's disease, huperzine A, polyhydroxyalkanoates, nanoparticle, neuroinflammation.

***Address for correspondence**: Daixu Wei, Zigong Institute of Brain Science, Zigong Psychiatric Research Center, Zigong Affiliated Hospital of Southwest Medical University, 643021 Zigong, Sichuan, China; Clinical Medical College and Affiliated Hospital of Chengdu University, Chengdu University, 610106 Chengdu, Sichuan, China. E-mail: weidaixu@cdu.edu.cn.

Introduction

Alzheimer's disease (AD), one of the most prevalent neurodegenerative disorders, affects over 57 million individuals globally and represents a major healthcare challenge exacerbated by population aging [1,2]. Its characteristic neuropathological features include extracellular β-amyloid (Aβ) plaque deposition, intracellular neurofibrillary tangles from hyperphosphorylated tau protein, and progressive neuronal loss [3,4]. Central cholinergic system dysfunction is central to AD cognitive decline [5]. The "Cholinergic Hypothesis of AD" posits that selective degeneration of basal forebrain cholinergic neurons directly causes a significant decline in cortical and hippocampal acetylcholine (ACh) levels, consequently disrupting synaptic plasticity, memory encoding, and attention regulation [5–7].

ACh dynamically regulates excitatory transmission

and synaptic remodeling within the corticolimbic circuitry by activating metabotropic muscarinic receptors (mAChRs) and ionotropic nicotinic receptors (nAChRs) [7]. Depletion of ACh exacerbates AD pathology through dual pathways: (1) Reduced ACh levels inhibit α-secretase activity, promoting aberrant cleavage of amyloid precursor protein (APP) to generate Aβ and accelerate senile plaque deposition [8]; (2) Aβ oligomers selectively damage basal forebrain cholinergic neurons by activating the Wnt/β-catenin signaling pathway, establishing a vicious positive feedback cycle of "ACh deficiency-Aβ accumulation" [9]. Clinical studies confirm abnormally elevated acetylcholinesterase (AChE) activity in the cerebrospinal fluid (CSF) of AD patients, accelerating ACh hydrolysis and worsening synaptic ACh deficiency. AChE inhibitors (AChEIs), which increase brain ACh levels to improve neurotransmission, constitute first-line therapy for mild-to-moderate AD [10]. However, conventional AChEIs (e.g., donepezil, rivastigmine, galantamine) are associated with adverse effects including gastrointestinal disturbances, bradycardia, and muscle cramps, while their clinical efficacy is limited by dose-dependent constraints [11,12]. Consequently, identifying safer and more effective AChEIs for AD treatment represents an urgent clinical need.

Huperzine A (HupA), a natural Lycopodiaceae alkaloid, has emerged as a research focus for AD treatment due to its potent, selective inhibition of central AChE, antioxidant properties, and neuroprotective effects [13]. Compared to synthetic AChEIs, HupA demonstrates superior blood-brain barrier (BBB) penetration and lower muscarinic receptor activation, highlighting its therapeutic potential for AD [13–15]. However, its short plasma half-life (~7 h) necessitates frequent dosing, potentially inducing dose-dependent side effects; long-term administration may also cause dizziness, bradycardia, and gastrointestinal disturbances [13,16,17]. While intravenous infusion or subcutaneous injection rapidly achieves systemic circulation of HupA, maintaining effective concentrations long-term remains challenging [18]. Recently, sustained-release nanoparticle (NP) systems based on biodegradable materials (e.g., PBVHx) offer a promising strategy to overcome this limitation.

PBVHx, the newest polyhydroxyalkanoate (PHA), is synthesized via synthetic biology platforms using engineered microorganisms. Composed of 3-hydroxybutyrate (3HB), 3-hydroxyvalerate (3HV), and 3-hydroxyhexanoate (3HHx), it exhibits excellent biocompatibility and controllable biodegradability [19,20]. Unlike analogous polyesters (e.g., PLA, PLGA), PBVHx and other PHAs degrade more slowly, producing non-toxic degradation by-product 3-hydroxybutyrate (3HB or BHB, pKa = 4.70). Compared to lactic acid (the degradation product of PLA/PLGA), 3HB is milder and induces less tissue irritation [21]. Notably, 3HB has been reported to inhibit inflammasome activation, potentially mitigating neuroinflammation in AD [21,22]. Furthermore, PBVHx typically achieves higher encapsulation efficiency (EE) for lipophilic drugs than PLA and its derivatives. Consequently, PHAs may represent superior carrier materials for AD therapeutics.

Given the outstanding properties of PBVHx, it has been engineered into diverse biomedical constructs—including micron/submicron spheres/particles, 3D scaffolds, and fibrous membranes—for drug delivery and tissue engineering [23,24]. We previously developed HupA-loaded PBVHx microspheres for AD treatment. These drug-loaded microspheres reduced HupA toxicity and enabled sustained release over 40 days, significantly improving cognitive function in AD model mice during *in vivo* studies [16]. However, compared to microspheres, nanoparticles possess smaller dimensions and enhanced tissue penetration capability, facilitating BBB transit and cellular internalization. This substantially increases drug accumulation in the brain and augments therapeutic efficacy [25]. Consequently, drug-loaded PBVHx nanoparticles exhibit unique advantages and promising therapeutic potential for AD management.

Owing to the amphiphilic nature of HupA, its encapsulation efficiency in either hydrophobic polyesters or hydrophilic hydrogel matrices is intrinsically low. Therefore, employing a delivery platform that integrates hydrophilic gel/hydrogel with hydrophobic polyester materials constitutes an effective strategy [26,27]. Given the systemic toxicity and poor patient compliance associated with frequent HupA administration, we developed a biphasic delivery platform composed of PHA nanoparticles embedded within a hyaluronic acid (HA) gel to enable sustained HupA release. It is particularly noteworthy that HA plays multiple critical roles in this system: its innate biocompatibility, hydrophilicity, and bioadhesive properties provide a stable and functional three-dimensional network for the nanoparticles, not only significantly improving drug loading efficiency but also enabling prolonged sustained release by modulating drug diffusion behavior [28]. Furthermore, HA possesses potential neurotrophic and barrier-repairing functions, thereby contributing to enhanced therapeutic outcomes [29]. Through this novel platform, we sought to overcome the currently limited encapsulation efficiency of HupA and to address the problems arising from its frequent dosing. Encouragingly, the platform achieved complete encapsulation of HupA. After a single administration, *in vivo* experiments demonstrated that the system significantly alleviated the pathological process of AD by inhibiting Aβ deposition, regulating neuroinflammation, suppressing neuronal apoptosis, and improving cognitive behavior, which positions HupA@(NP/Gel) as a highly promising novel subcutaneous delivery platform for AD therapy.

Table 1. Antibody information.

Antibody name	Company	Origin	Catalog No	Dilution
GFAP	Cell Signaling Technology	USA	#80788	IF:1:200; WB:1:1000
Iba1	Cell Signaling Technology	USA	#17198	IF:1:200; WB:1:1000
NeuN	Cell Signaling Technology	USA	#A6NFN3	IF:1:200; WB:1:1000
NfL	Cell Signaling Technology	USA	#2837	IF:1:200; WB:1:1000
cleaved-caspase 3	Affinity	China	#AF7022	IF:1:200; WB:1:1000
CD68	Cell Signaling Technology	USA	#97778	WB:1:1000
Bax	Affinity	China	#AF0120	WB:1:1000
Bcl-2	Abcam	UK	ab182858	WB:1:2000
APP	Affinity	China	#AF6084	WB:1:1000
$A\beta_{1-42}$	Biolegend	USA	# SIG-39142	WB:1:500
IL-6	Abcam	UK	ab290735	WB:1:1000
P-Tau	Abmart	China	T59003	WB:1:1500
Tau	Abmart	China	T55846	WB:1:2000
IL-1β	Abcam	UK	ab283818	WB:1:1000
TNF-α	Sabbiotech	USA	#29084	WB:1:1000
GAPDH	Bioss	China	bsm-52262R	WB:1:20000

Materials and Methods

Materials

Medical poly (3-hydroxybutyrate-co-3-hydroxyvalerate-co-3-hydroxyhexanoate) (PBVHx or PHBVHHx, weight-average molecular weight 26,000 Da, with 85 mol% 3HB, 2% 3HV, and 12% 3HHx) was purchased from Bluepha Co., Ltd. (China). Hyaluronate sodium (H874944) was supplied by Shanghai Macklin Biochemical Co., Ltd. (China). HupA (H420384) and polyvinyl alcohol (PVA, 87–89% alcoholysis degree, weight-average molecular weight 13,000~23,000 Da, P434367) were obtained from Aladdin (China). Dichloromethane (DCM) and other routine chemical reagents (analytical grade) were supplied by Sinopharm Chemical Reagent Co., Ltd. (China). Tunel Staining Kit (P-CA-301) was provided by Pricella Biotechnology Co., Ltd. (China). Polyvinylidene Fluoride Membrane (PVDF, IPVH00010) was acquired from Merck Millipore (Germany). RIPA buffer (R0010), Micro AChE Assay Kit (BC2025), BCA Protein Assay Kit (PC0020), TBST (T1081), and NON-Fat Powdered Milk (D8340) were from Solarbio (China). The primary antibodies were purchased from multiple biotechnology companies (Table 1). Secondary antibodies (bs-0295G and bs-0296G) were sourced from Bioss (China). $A\beta_{25-35}$ (A4559) and D-galactose (G0750) were provided by Sigma-Aldrich (USA).

Preparation of HupA@NPs and HupA@(NP/Gel)

As an amphiphilic drug, HupA is soluble in both organic solvents and water, leading to low loading efficiency in either hydrophobic polyester or hydrophilic hydrogel systems. To address this, we designed a novel nanoparticle-gel composite capable of achieving 100% HupA loading. An improved oil-in-water (O/W) emulsification method based on ultrasonic fragmentation was employed, allowing most of the HupA to be loaded into PBVHx nanoparticles (HupA@NPs). HA was further added to encapsulate any remaining unloaded HupA. Briefly, varying amounts of PBVHx (2, 4, and 6 g) and HupA (0.5 g) were dissolved in 100 mL DCM as the oil phase, corresponding to PBVHx concentrations of 2%, 4%, and 6%, respectively. The PBVHx/DCM solution was mixed with 0.1% PVA at a 1:10 volume ratio and emulsified via ultrasonic fragmentation in an ice bath. The DCM was then evaporated using a rotary evaporator (Shanghai Yukang Scientific Instrument Inc.) at room temperature (RT) for 5–7 min to solidify the PBVHx nanoparticles, yielding HupA@NPs. The solution was adjusted to its original volume with ddH_2O, followed by the addition of HA at final concentrations of 1%, 2%, and 4% to obtain HupA@(NP/Gel).

Characterization of HupA@NPs and HupA@(NP/Gel)

The morphology of HupA@NPs was observed using transmission electron microscopy (TEM, 1200EX instrument JEM, Japan). The microstructure of HupA@(NP/Gel) was examined via scanning electron microscopy (SEM, Hitachi S-4800, Japan) at an accelerating voltage of 12 ~ 15 kV. The particle size and surface charge of HupA@NPs and control groups were measured at 25°C using a Malvern Particle Size Analyzer (Mastersizer 3000, Malvern Instruments, UK), with samples dispersed in pure water. The Fourier transform infrared (FTIR) spectra of HupA@NPs, HupA@(NP/Gel), and HupA@Gel were analyzed using a PerkinElmer RX1 FTIR spectrometer (Nicolet 6700, Thermo Scientific, USA) over the wavenumber range of 4000–400 cm^{-1} to confirm the presence of chemical functional groups.

Encapsulation Efficiency of HupA

The EE of HupA in HupA@NPs was determined by HPLC after centrifugation. Briefly, a known mass of NPs was dissolved in DCM, and free HupA (W1) was collected by filtration. The sample was then dissolved in methanol (*v*/*v* = 1:1) and analyzed by HPLC (Agilent, USA) at a flow rate of 0.8 mL/min with UV detection at 310 nm. The theoretical total HupA input was denoted as W0. The EE was calculated using Equation (1), and each sample was tested in triplicate.

$$\text{EE of HupA}(\%) = (\text{W0} - \text{W1}/\text{W0}) \times 100\% \quad (1)$$

In Vitro Drug Release Assay

The dried HupA@NPs, HupA@(NP/Gel), and HupA@Gel samples (100 mg each) were immersed in 10 mL of medium (PBS buffer containing 0.1 mg/mL lipase, pH 7.4) and incubated at 37°C for 20 days. The medium was replaced with fresh solution every 2 days to maintain enzyme activity. At predetermined time points, the medium was collected and then quantified using HPLC. The cumulative release of HupA was calculated using Equation (2):

$$\text{Cumulative release of HupA}(\%) = (\text{W2}/\text{W3}) \times 100 \quad (2)$$

where W2 represents the relative released amount of HupA and W3 denotes the total amount of HupA in samples.

AD Mice and Treatment

8-week-old male C57BL/6 mice (body weight range 22–28 g) were commercially acquired from GemPharmatech (Chengdu, China). Animals were maintained under controlled environmental conditions (24 ± 1°C, 45–65% humidity, 12 h light/dark cycle) with ad libitum access to food and water. Only healthy mice were included in the study following a one-week acclimatization period, which served to exclude those with visible behavioral abnormalities or signs of disease. Furthermore, any animals that failed to meet the established model criteria or reached predefined humane endpoints during the modeling or experimental phases were excluded from the final analysis. All experimental protocols involving animals were approved by the Ethics Committee of Zigong Mental Health Center (Ethics Approval No. ZPRC-20240523) and conducted in strict accordance with the National Research Council's Guidelines for the Care and Use of Laboratory Animals in China. Every effort was made to minimize pain and distress throughout the experimental procedures.

D-Galactose was dissolved in sterile saline, filtered through a 0.22 μm membrane, and the stock solution was prepared at a concentration of 10 mM. Aβ_{25-35} was dissolved in deionized water, incubated with constant agitation at 37°C for 72 h to induce fibrillar aggregation, and adjusted to a final concentration of 1 mM as a stock solution. HupA was initially dissolved in a minimal volume of DMSO, completely dissolved via vortexing, and then diluted with sterile saline to prepare a stock solution at a final concentration of 5 mg/mL. All stock solutions were aliquoted and stored at –20°C to avoid repeated freeze-thaw cycles, and freshly diluted to the desired concentrations prior to experimental application.

Following acclimatization, forty-eight mice were randomly assigned to four groups (n = 12 per group) using a computer-generated random number sequence: control, HupA@(NP/Gel), free-HupA, and AD. All groups except the control received daily intraperitoneal injections of D-galactose (100 mg/kg/day; i.p.) for 8 weeks, whereas the control group was administered sterile saline for an equivalent duration. At week 9, all animals underwent stereotaxic surgery. Anesthetized mice were immobilized in a stereotaxic frame, and the CA1 hippocampal region was stereotaxically targeted for injection. Bilateral intracerebroventricular injections of Aβ_{25-35} (4 μL) were administered to experimental groups following established protocols, whereas the NC group received equivalent-volume sterile saline. Stereotaxic infusion parameters included: needle insertion rate (0.02 mm/s), infusion rate (0.8 μL/min), post-injection needle retention (5 min for complete drug diffusion), and withdrawal rate (0.01 mm/s) [30,31]. Post-procedural craniotomy sites were surgically sealed with dental cement bilaterally, followed by layered closure of the surgical incision. All mice underwent a one-week postoperative recovery period prior to drug administration commencing at week 10. Mice in the HupA@(NP/Gel) and free-HupA groups received i.p. injections of HupA@(NP/Gel) or free HupA, respectively, with both groups administered equivalent HupA doses (0.2 mg/kg). Mice in the control and AD groups were administered equivalent volumes of sterile saline.

Animal Behavioral Tests

Mice were sequentially subjected to the open field test (OFT), elevated plus maze (EPM), novel object recognition (NOR), and Morris water maze (MWM) assessments. A 24 h rest interval was implemented between each of these consecutive behavioral tests to prevent fatigue and carryover effects. A 30-min laboratory acclimatization period was implemented for mice prior to behavioral testing. The apparatus was decontaminated with 75% ethanol (*v*/*v*) between trials to eliminate odor cues [32,33].

The OFT apparatus was constructed as a 40 × 40 × 40 cm^3 enclosure featuring a 20 × 20 cm^2 designated central quadrant. Mice were centrally positioned, and locomotor activity was video-tracked for 5 min.

The EPM apparatus comprised two open arms (30 × 8 cm^2), two enclosed arms (30 × 8 × 15 cm^3), and a central platform (8 × 8 cm^2). Individual mice were positioned on the central platform oriented toward an open arm.

Open/closed arm entries and dwell times were quantified during a 5 min trial.

The NOR test was conducted in an open field arena. The experiment comprised three sequential phases: habituation, training, and testing. During the habituation phase, mice were individually placed in the arena and allowed to freely explore for 10 min to reduce anxiety toward the novel environment. In the training phase, two identical objects were symmetrically positioned at the center of the arena. Mice were gently introduced from a corner and permitted to explore for 10 min, with exploratory behavior recorded. 1 h post-training, the testing phase commenced by replacing one familiar object with a novel object. Mice were then allowed to explore freely for 10 min, during which exploration times for both objects were quantified.

The spatial learning and memory of mice were assessed using a MWM consisting of a circular pool (120 cm diameter) divided into four quadrants, with a submerged platform (4.5 × 4.5 cm^2) placed 1 cm below the water surface in the target quadrant and visual cues affixed to the surrounding walls as spatial references. Over a 6-day protocol, mice underwent daily acquisition training (Days 1–5) comprising four trials with 1 h inter-trial intervals, where they were released from randomized entry points and allowed 90 seconds to locate the hidden platform; escape latency (time to platform discovery) was recorded, and unsuccessful trials concluded with guided platform exposure for 10 seconds. On Day 6, a probe trial was conducted by removing the platform and allowing 90 seconds of free exploration, during which trajectory heatmaps, virtual escape latency, target quadrant occupancy time, and crossing frequency were quantified via an overhead video-tracking system (EthoVision XT, Noldus) to evaluate spatial memory retention.

AChE Activity Detection

To assess the AChE activity in each group of mice, an AchE activity assay kit was used. Fresh hippocampal tissues of mice were separated and homogenised on ice after the addition of the extract, and the supernatant was collected for testing after centrifugation. Subsequent operations were carried out according to the manufacturer's protocol, and then the absorbance of the supernatant at 412 nm was detected by using a microplate reader.

Immunofluorescence

Upon completion of behavioral testing, mice were deeply anesthetized with 3% isoflurane in an induction chamber until the loss of righting reflex, followed by cervical dislocation to ensure euthanasia. Brains were rapidly harvested, followed by fixation and dehydration prior to cryosectioning. Coronal brain sections (10 μm thickness) were prepared for immunofluorescence staining. Sections underwent permeabilization with 0.5% Triton X-100 in PBS for 20 min, followed by three PBS washes. Nonspecific binding was blocked with 5% BSA-PBS for 40 min at RT. Primary antibodies (Table 1) were applied and incubated overnight at 4°C. After three PBS washes, sections were incubated with fluorophore-conjugated secondary antibodies for 2 h at RT. Nuclei were counterstained with DAPI (15 min, RT), and images were captured using a Nikon C2 confocal microscope (Japan). Fluorescence intensity was quantified via ImageJ software.

HE Staining

For HE staining, fixed tissue samples (heart, liver, spleen, lung, and kidney) were dehydrated through a graded ethanol series, embedded in paraffin, and sectioned at 5 μm. Following dewaxing and rehydration, sections were stained with hematoxylin for 3–5 min, differentiated in acid ethanol, blued in ammonia water, and rinsed. Subsequent dehydration was performed in 85% and 95% ethanol, followed by counterstaining with eosin. Finally, sections were cleared in xylene, mounted with neutral balsam, and imaged under an inverted microscope for analysis.

Protein Extraction and Western Blot

Hippocampal proteins were extracted using RIPA lysis buffer supplemented with protease inhibitors. Protein concentrations were quantified via the BCA assay. Samples were separated by SDS-PAGE and transferred to PVDF membranes. Membranes were blocked with 5% nonfat milk in TBST (1 h, RT) and incubated overnight at 4°C with primary antibodies (Table 1). After three TBST washes, membranes were incubated with HRP-conjugated secondary antibodies (2 h, RT). Protein bands were visualized using an ECL substrate and imaged with a Vilber FUSION Fx6 system. Band intensity was quantified using ImageJ software.

Tunel Staining

Following established protocols from prior research and the Tunel staining kit guidelines, 10-μm-thick brain sections underwent sequential processing steps: permeabilization, equilibration, labeling, nuclear staining, and coverslipping. Neuronal apoptosis was examined using confocal microscopy, with apoptotic cells in different brain regions quantified through ImageJ software analysis.

Transcriptome Sequencing

Total RNA was extracted from the hippocampal tissues of mice in the HupA@(NP/Gel) and AD groups, followed by storage at –80°C for subsequent analysis. Transcriptomic libraries were constructed using the VAHTS Universal V5 RNA-seq Library Prep Kit (Vazyme) according to the manufacturer's instructions. Sequencing was performed on the Illumina NovaSeq 6000 platform. Subsequent transcriptome sequencing and bioinformatic analysis were conducted by Shanghai OE Biotech Co., Ltd.

Statistical Analysis

Quantitative data were expressed as mean ± standard deviation (SD). The normality of data distribution was assessed using the Shapiro-Wilk test, and the homogeneity of variances was verified using Levene's test. All datasets met the assumptions for parametric analysis. Statistical analyses were conducted using SPSS 20.0 (IBM), with intergroup comparisons performed via one-way ANOVA followed by Tukey's post hoc test. Significance thresholds were defined as $*p < 0.05$, $**p < 0.01$, $***p < 0.001$ and $****p < 0.0001$.

Results

Preparation, Optimization, and Characterization of HupA@NPs

As shown in Fig. 1**A**, HupA@NPs were prepared from HupA and PBVHx via ultrasonic emulsification. By varying the PBVHx concentration in DCM, we prepared HupA@2%NP, HupA@4%NP, HupA@6%NP, and nanoparticles (4%NP) without HupA (Fig. 1**B**). HPLC analysis determined the EE of the drug-loaded nanoparticles. At 4% PBVHx concentration, HupA@4%NP exhibited the highest EE (50.26%), significantly exceeding those of HupA@2%NP (23.73%) and HupA@6%NP (44.05%) ($p < 0.05$; Fig. 1**E**). Size distributions, measured by Malvern particle size analysis (Fig. 1**D**), demonstrated a progressive increase in nanoparticle size as PBVHx concentration rose from 2% to 6%. However, at fixed PBVHx concentrations, drug loading had no significant impact on size distribution (Fig. 1**D**). Transmission electron microscopy (TEM) characterized the morphology of all four nanoparticle types (Fig. 1**C**). Most nanoparticles appeared spherical or ellipsoidal, with size distributions consistent with Malvern measurements. The zeta potentials of all four nanoparticle types ranged between –20 mV and –25 mV, showing no significant differences, indicating that neither drug loading nor PBVHx content markedly affected surface charge (Fig. 1**F**). Based on these results, HupA@4%NP, possessing the highest EE, was selected for subsequent studies. FTIR spectroscopy further confirmed successful HupA loading (Fig. 1**G**). Compared to 4%NP, HupA@4%NP exhibited characteristic HupA peaks: pyridone ring breathing vibrations at 1603 cm^{-1} and 1665 cm^{-1}, along with significantly enhanced intensity of the C=O stretching vibration at 1789 cm^{-1} and the N–H stretching vibration at 3470 cm^{-1}.

Preparation and Characterization of HupA@(NP/Gel)

To overcome HupA's limited aqueous solubility, we designed a novel nanoparticle-gel system to achieve 100% HupA loading. As illustrated in Fig. 1**A**, HupA@NPs were prepared via ultrasonic emulsification. After DCM evaporation, HA solutions (1%, 2%, 4%) were introduced to form composite drug-loaded nanoparticle-gel systems (HupA@(NP/Gel)). Tube inversion tests revealed progressively reduced flowability in the composites with increasing HA concentration (Fig. 1**H**). SEM (Fig. 1**J**) showed HupA@NPs distributed within the HA matrix (indicated by red arrows). FTIR spectroscopy of HupA@NPs, HupA@(NP/4%Gel), and 4%Gel confirmed successful incorporation: spectral changes in HupA@(NP/4%Gel) around ~1600 cm^{-1} (overlap region of HA amide I N-H bending and HupA pyridone ring vibrations) indicated nanoparticle embedding. Simultaneously, the appearance of a characteristic HA amide absorption peak near ~600 cm^{-1} further verified HA presence. Furthermore, the prominent HupA-derived C=O stretching vibration peak at ~1780 cm^{-1} in HupA@NPs spectra was significantly attenuated or absent in HupA@(NP/4%Gel), suggesting masking effects by the HA matrix. Collectively, these FTIR spectral shifts confirm the successful loading of HupA@NPs within the HA matrix (Fig. 1**I**).

Release Profile Determination and Optimization of HupA@(NP/Gel)

The introduction of HA gel matrix may result in a two-stage drug release pattern: an initial rapid release phase of HupA from the HA gel matrix, followed by a sustained release phase as HupA diffuses from degrading PBVHx nanoparticles (Fig. 2**J**). To validate this, HupA release profiles from HupA@NPs, HupA@Gel, and HupA@(NP/Gel) were determined via HPLC (Fig. 2**A–C**). As shown in Fig. 2**D**, HupA@2%NP, HupA@4%NP, and HupA@6%NP all exhibited sustained HupA release over 20 days with similar release kinetics, indicating minimal influence of PBVHx concentration on the release pattern. However, HupA@4%NP demonstrated higher cumulative release than HupA@2%NP and HupA@6%NP at equivalent time points, consistent with its superior EE ($p < 0.05$; Fig. 2**E**). Release from HupA@Gel systems (Fig. 2**E**) showed prolonged release duration with increasing HA concentration: HupA@1%Gel (~2 days), HupA@2%Gel (~4 days), and HupA@4%Gel (~6 days). Critically, release profiles from HupA@(NP/Gel) composites (Fig. 2**F**) revealed that increasing the HA gel concentration (at fixed PBVHx concentration) yielded more gradual release kinetics. This significantly extends *in vivo* drug release duration while mitigating the initial burst release-associated toxicity.

To visually demonstrate the biphasic release profile (Fig. 2**J**) and the HA concentration-dependent modulation of HupA release kinetics, the release profiles from Fig. 2**D–F** were replotted as shown in Fig. 2**G–I**. Taking Fig. 2**I** as an example, the three curves represent HupA release from 4%NP, HupA@4%Gel, and HupA@(4%NP/4%Gel), respectively. Release from HupA@4%Gel lasted about 6 days. Notably, the release profiles of HupA@4%Gel and HupA@(4%NP/4%Gel) nearly overlapped during the first 6 days. This indicates that HupA release from HupA@(4%NP/4%Gel) in this initial phase originated primarily from the rapid release of HupA within the HA

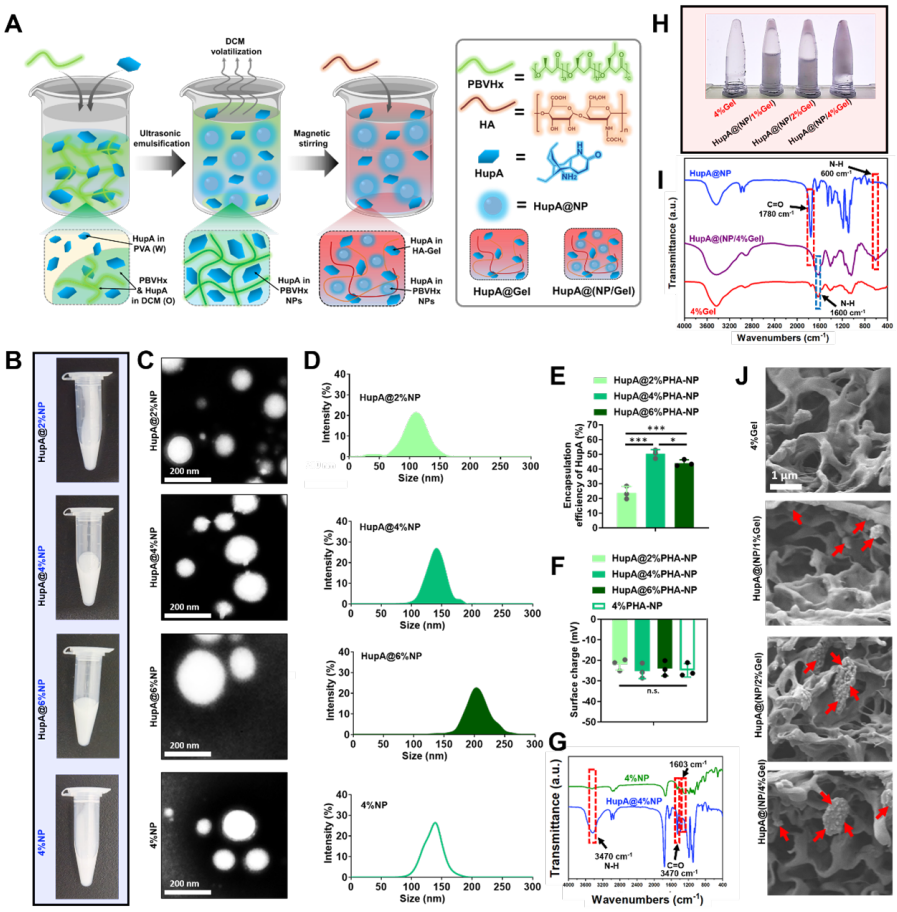

Fig. 1. Preparation and characterization of HupA@NP and HupA@(NP/Gel). (**A**) Schematic illustrating the preparation of HupA@NP and HupA@(NP/Gel). HupA@NP was prepared by ultrasonic emulsification. HupA@(NP/Gel) was formed by introducing hyaluronic acid into HupA@NP after dichloromethane evaporation. The system achieved 100% drug loading with HupA partially loaded in the hyaluronic acid gel and the remainder incorporated within PBVHx nanoparticles. (**B**) Photographs of HupA@2%NP, HupA@4%NP, HupA@6%NP and 4%NP. (**C**) Representative TEM images of HupA@2%NP, HupA@4%NP, HupA@6%NP and 4%NP. The scale bar represents 200 nm. (**D**) Size distribution profiles of HupA@2%NP, HupA@4%NP, HupA@6%NP and 4%NP. (**E**) Encapsulation efficiency of HupA in HupA@2%NP, HupA@4%NP and HupA@6%NP. (**F**) Zeta potential values of HupA@2%NP, HupA@4%NP, HupA@6%NP and 4%NP. (**G**) FTIR spectra of HupA@4%NP and 4%NP. (**H**) Vial inversion images of 4%Gel, HupA@(NP/1%Gel), HupA@(NP/2%Gel) and HupA@(NP/4%Gel). (**I**) FTIR spectra of HupA@NP, HupA@(NP/4%Gel) and 4%Gel. (**J**) SEM images of 4%Gel, HupA@(NP/1%Gel), HupA@(NP/2%Gel) and HupA@(NP/4%Gel). The scale bar represents 1 μm. Data presented as mean ± SD (n = 3). *$p < 0.05$ and ***$p < 0.001$. Among them, Fig. 1A was drawn using Microsoft PowerPoint.

matrix, not from the PBVHx nanoparticles. Following HA degradation and complete release of its encapsulated HupA after day 6, sustained release transitioned to HupA diffusion from the degrading PBVHx nanoparticles, extending for up to 20 days. Similarly, Fig. 2**G** and Fig. 2**H** demonstrate that Phase I release lasted about 1.5 days for HupA@(4%NP/1%Gel) and 4 days for HupA@(4%NP/2%Gel), with both exhibiting shorter Phase II durations compared to HupA@(4%NP/4%Gel). Crucially, HupA@(4%NP/4%Gel) displayed significantly more gradual release kinetics, particularly during Phase I, effectively mitigating the burst release-associated toxicity observed with lower HA concentrations. Based on these findings, HupA@(4%NP/4%Gel) (designated HupA@(NP/Gel)) was selected for subsequent *in vivo* efficacy evaluation.

HupA@(NP/Gel) Ameliorates Anxiety-like Behavior and Spatial Memory Deficits in AD Mice

To assess the impact of HupA@(NP/Gel) on anxiety-like behavior and spatial memory in AD mice, behavioral tests were performed after 21 days of treatment. OFT heatmaps showed uniform exploration in control and HupA@(NP/Gel) groups, but thigmotaxis in free-HupA and AD groups (Fig. 3**A**). AD mice exhibited reduced center entries and duration; HupA@(NP/Gel) significantly increased these measures versus AD and free-HupA groups ($p < 0.05$; Fig. 3**B–D**). EPM heatmaps revealed AD mice confined to one closed arm, free-HupA mice moving between closed arms, while control and HupA@(NP/Gel)

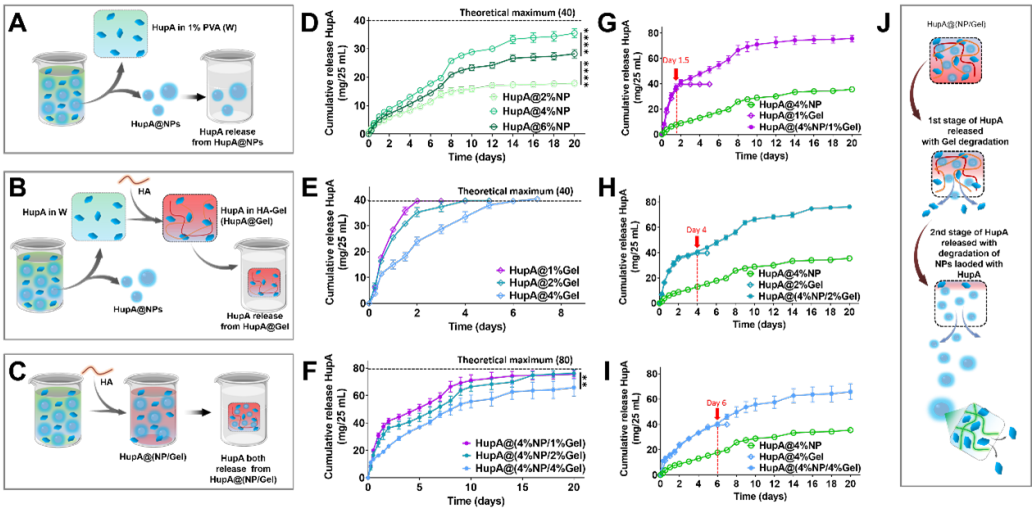

Fig. 2. Release profiles and mechanism of HupA@(NP/Gel). (**A–C**) Schematic representations of HupA release from HupA@NPs, HupA@Gel and HupA@(NP/Gel), respectively. (**D**) Release profiles of HupA@2%NP, HupA@4%NP and HupA@6%NP. (**E**) Release profiles of HupA@1%Gel, HupA@2%Gel and HupA@4%Gel. (**F**) Release profiles of HupA@(4%NP/1%Gel), HupA@(4%NP/2%Gel) and HupA@(4%NP/4%Gel). (**G**) Release profiles of HupA@(4%NP/1%Gel), HupA@1%Gel and HupA@4%NP. Distinct release profiles between HupA@(4%NP/1%Gel) and HupA@1%Gel emerge after day 1.5. (**H**) Release profiles of HupA@(4%NP/2%Gel), HupA@2%Gel and HupA@4%NP. Distinct release profiles between HupA@(4%NP/2%Gel) and HupA@2%Gel emerge after day 4. (**I**) Release profiles of HupA@(4%NP/4%Gel), HupA@4%Gel and HupA@4%NP. Distinct release profiles between HupA@(4%NP/4%Gel) and HupA@4%Gel emerge after day 6. (**J**) Schematic two-phase release pattern: Phase I-HupA release accompanying HA gel degradation; Phase II-HupA release accompanying NP degradation. Data presented as mean ± SD (n = 3). $^{**}p < 0.01$ and $^{****}p < 0.0001$. Among them, Fig. 2A, 2B, 2C and 2J were drawn using Microsoft PowerPoint.

groups explored open arms (Fig. 3**E**). AD mice showed fewer open arm entries and less time; HupA@(NP/Gel) increased both ($p < 0.05$; Fig. 3**F–H**). OFT/EPM results indicate HupA@(NP/Gel) ameliorated anxiety-like behavior. During MWM training, AD and free-HupA mice had longer escape latencies than control and HupA@(NP/Gel) groups ($p < 0.05$; Fig. 3**J**). In the probe test, AD and free-HupA mice swam randomly, while HupA@(NP/Gel) mice preferentially explored the target quadrant (Fig. 3**I**). AD mice had fewer platform crossings and less target quadrant time; free-HupA showed non-significant improvement, while HupA@(NP/Gel) significantly increased both ($p < 0.01$; Fig. 3**K** and **L**). NOR showed lower recognition indices in free-HupA and AD groups versus control; HupA@(NP/Gel) improved this index in AD mice ($p < 0.01$; Fig. 3**M** and **N**). MWM and NOR results demonstrate that the HupA@(NP/Gel) improved spatial memory deficits.

HupA@(NP/Gel) Modulates the Cholinergic System and Prevents Aβ Deposition in AD Mice

To determine whether a single injection of HupA@(NP/Gel) or free-HupA protects cholinergic neurons in AD mice, we assessed changes in AChE activity and choline acetyltransferase (ChAT) protein concentration in mouse brains 21 days post-administration. HupA@(NP/Gel) treatment significantly reduced AChE activity to levels approaching those in normal controls, markedly lower than in both free-HupA and AD groups ($p < 0.001$; Fig. 4**A**). This indicates that HupA@(NP/Gel) functioned as an AChE inhibitor. Conversely, ChAT protein expression was significantly higher after HupA@(NP/Gel) treatment compared to free-HupA treatment ($p < 0.001$; Fig. 4**B** and **C**). This demonstrates that HupA@(NP/Gel) enhances ACh synthesis by promoting ChAT expression, thereby ensuring cholinergic neurotransmission.

Amyloid-β (Aβ) deposition is a hallmark pathology in AD [2]. In this study, accelerated aging was induced in mice via 8-week intraperitoneal injection of D-galactose, while Aβ deposition was modeled by intracerebroventricular injection of $A\beta_{25-35}$ peptide. To assess whether a single injection of HupA@(NP/Gel) modulates key AD-related proteins, we quantified the expression of APP and Aβ. Both APP and Aβ levels were significantly elevated in AD model mice. While a single injection of free-HupA significantly reduced APP and Aβ expression in AD mice, this reduction was less pronounced than that achieved with HupA@(NP/Gel) ($p < 0.001$; Fig. 4**D–F**). In addition, HupA@(NP/Gel) treatment significantly reduced the P-Tau/Tau ratio compared with the AD group ($p < 0.001$; Fig. 4**G** and **H**). These results indicate that the sustained release of HupA from HupA@(NP/Gel) effectively downregulates APP expression and attenuates Aβ deposition.

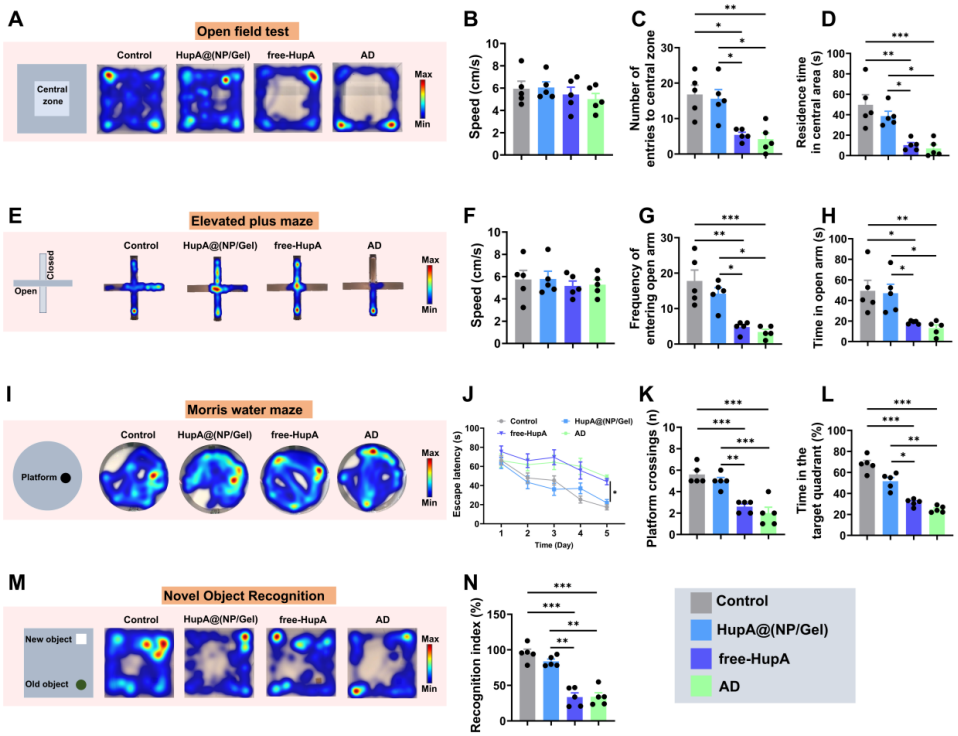

Fig. 3. HupA@(NP/Gel) treatment ameliorates anxiety-like behaviors and spatial memory in AD mice. (**A**) Representative heat maps of the OFT. (**B**) Locomotion speed in OFT. (**C**) Frequency of the entered central area of the open field. (**D**) Residence time in the central area of the open field. (**E**) Representative heat maps of EPM. (**F**) Locomotion speed in EPM. (**G**) Frequency of entered in the open arm of the EPM. (**H**) Residence time in the open arm of the EPM. (**I**) Representative heat maps of the MWM. (**J**) Escape latency during the training period in MWM. (**K**) Platform crossings in MWM. (**L**) Time in the target quadrant. (**M**) Representative heat maps of the NOR. (**N**) Recognition index.Data presented as mean ± SD (n = 5). *$p < 0.05$, **$p < 0.01$ and ***$p < 0.001$.

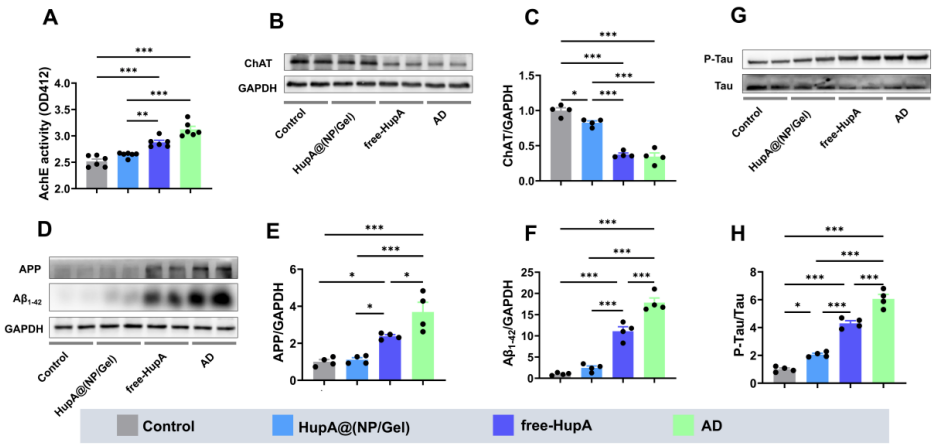

Fig. 4. HupA@(NP/Gel) treatment modulates the acetylcholine system and prevents Aβ deposition. (**A**) AChE activity (n = 6). (**B**) Representative Western blots of hippocampal ChAT protein. (**C**) Quantification of ChAT protein expression. (**D**) Representative Western blots of hippocampal APP and Aβ_{1-42} proteins. (**E**) Quantification of APP protein expression. (**F**) Quantification of Aβ_{1-42} protein expression. (**G**) Representative Western blots of hippocampal P-Tau and Tau proteins. (**H**) P-Tau/Tau ratio (n = 4). Data presented as mean ± SD. *$p < 0.05$, **$p < 0.01$ and ***$p < 0.001$.

HupA@(NP/Gel) Effectively Attenuates Hippocampal Neuroinflammation in AD Mice

During AD progression, Aβ deposition activates microglia and astrocytes [34]. To evaluate the effect of HupA@(NP/Gel) on astrocyte and microglial activity in AD mice, we assessed the distribution and expression of the astrocyte marker GFAP and the microglial marker Iba1. Immunofluorescence revealed significantly elevated GFAP (Fig. 5**A**) and Iba1 (Fig. 5**F**) expression in the hippocampus of AD mice. While a single injection of

free-HupA reduced expression of both markers, the effect was less pronounced than with HupA@(NP/Gel). Subsequent analysis of hippocampal subregions (CA1, CA3, DG) showed consistently elevated expression in AD mice across all areas. HupA@(NP/Gel) treatment effectively attenuated this aberrant expression in each subregion ($p < 0.001$; Fig. 5**B–E** and **G–J**). WB analysis further confirmed these trends (Fig. 5**K**): the expression of GFAP and Iba1 in the hippocampus of the AD group was significantly increased. Free-HupA partially suppressed this increase, whereas HupA@(NP/Gel) treatment produced a more substantial reduction ($p < 0.001$; Fig. 5**L** and **M**). Additionally, expression of the M1 microglial marker CD68 followed a similar trend to Iba1($p < 0.001$; Fig. 5**N**). Collectively, these results demonstrate that HupA@(NP/Gel) treatment effectively prevents aberrant activation of astrocytes and microglia in AD mice.

Aberrantly activated astrocytes and microglia are key instigators of cerebral cytokine storms, directly driving neuroinflammation through pro-inflammatory cytokine release [34]. To assess the impact of HupA@(NP/Gel) treatment on hippocampal inflammation in AD mice, we quantified protein expression levels of pro-inflammatory cytokines (IL-1β, IL-6, TNF-α in hippocampal tissue via Western blotting. Results showed significantly elevated levels of IL-1β, IL-6, and TNF-α in AD mice. While free-HupA treatment reduced IL-1β and IL-6 expression, HupA@(NP/Gel) treatment restored levels of all three cytokines to near-normal values ($p < 0.001$; Fig. 5**O–Q**). These levels were significantly lower than those in both the AD and free-HupA groups, demonstrating that HupA@(NP/Gel) effectively prevents neuroinflammation in the AD hippocampus.

To further investigate differential biological signaling between HupA@(NP/Gel)-treated and AD model mice, we performed reference-based transcriptome sequencing on hippocampal tissues. Sequencing identified 508 differentially expressed genes (DEGs), with 211 significantly upregulated and 297 downregulated (Fig. 6**A**). DEGs filtered (p-value < 0.05 and $|\log2\ FC| > 1$) included Nox1 (oxidative stress), Cxcl10 (immune regulation), Pou4f2 and Glp1r (neuronal function), and hemoglobin subunit Hbb-bt, suggesting HupA@(NP/Gel) modulates oxidative stress, immune response, and neural function pathways (Fig. 6**B**). Gene set enrichment analysis (GSEA) revealed significant positive enrichment (NES = 2.0, FDR = 0.009) for "DNA-binding transcription factor activity" (GO:0003700), indicating transcription factor networks drive coordinated changes in downstream pathways (e.g., cell proliferation, stress response) (Fig. 6**C**). KEGG analysis showed AD-associated pathways played central roles: significant enrichment of oxidative phosphorylation and involvement of complement/coagulation cascades implicated mitochondrial dysfunction and neuroinflammation as AD drivers (Fig. 6**D**). Violin plot analysis confirmed strong associations between AD and oxidative phosphorylation/core neurodegenerative mechanisms (e.g., dysregulated mitochondrial energetics, oxidative stress), suggesting AD progression is synergistically driven by mitochondrial dysfunction and reactive oxygen species (ROS) accumulation (Fig. 6**E**). HupA@(NP/Gel) treatment counteracted these by modulating energy metabolism and suppressing neuroinflammation.

Furthermore, H&E staining revealed unremarkable histological architecture in all examined organs—heart, liver, spleen, lung, and kidney—across treatment groups. Specifically, cardiac tissue exhibited well-aligned cardiomyocytes with distinct striations; hepatic lobules maintained structural integrity; splenic red and white pulp compartments were clearly delineated; pulmonary alveoli remained intact; and renal glomeruli and tubules showed normal morphology. No significant pathological changes were observed in any group (Fig. 7). These findings demonstrate that HupA@(NP/Gel) exhibits favorable biocompatibility.

HupA@(NP/Gel) Exerts Neuroprotective and Anti-Apoptotic Effects

Progressive neuronal loss characterizes AD pathogenesis [35]. To evaluate whether HupA@(NP/Gel) treatment exerts neuroprotective effects on neuronal survival, we first assessed expression of the mature neuronal marker NeuN. Results revealed significantly reduced NeuN expression in the hippocampus of both AD model mice and free-HupA-treated mice, with diminished fluorescence intensity in the CA1, CA3, and DG subregions. In contrast, HupA@(NP/Gel) treatment increased NeuN protein expression ($p < 0.05$; Fig. 8**A–E**). Consistent with these observations, WB analysis confirmed that a single injection of HupA@(NP/Gel) significantly elevated NeuN levels in the AD mouse hippocampus ($p < 0.01$; Fig. 8**F** and **G**). These findings indicate that sustained HupA release from HupA@(NP/Gel) effectively enhances neuronal survival in the AD hippocampus.

Neurofilament light chain (NfL), a biomarker of axonal damage, is closely associated with AD progression [36]. Its abnormal accumulation may be directly driven by tau-mediated axonal transport deficits or Aβ-induced neuronal toxicity in AD. To assess axonal loss in AD mice, we measured NfL protein expression. Results revealed a significant surge in hippocampal NfL levels in AD mice. While a single free-HupA injection moderately reduced NfL expression, this reduction was less pronounced than that achieved with a single HupA@(NP/Gel) administration ($p < 0.001$; Fig. 8**H–L**). Consistent with expectations, WB analysis further confirmed that HupA@(NP/Gel) treatment effectively lowered hippocampal NfL levels in AD mice ($p < 0.001$; Fig. 8**M** and **N**). These findings indicate that sustained HupA release from HupA@(NP/Gel) effectively mitigates axonal damage in AD.

Increased neuronal apoptosis underlies hippocampal neuron loss in AD mice [35]. To evaluate whether

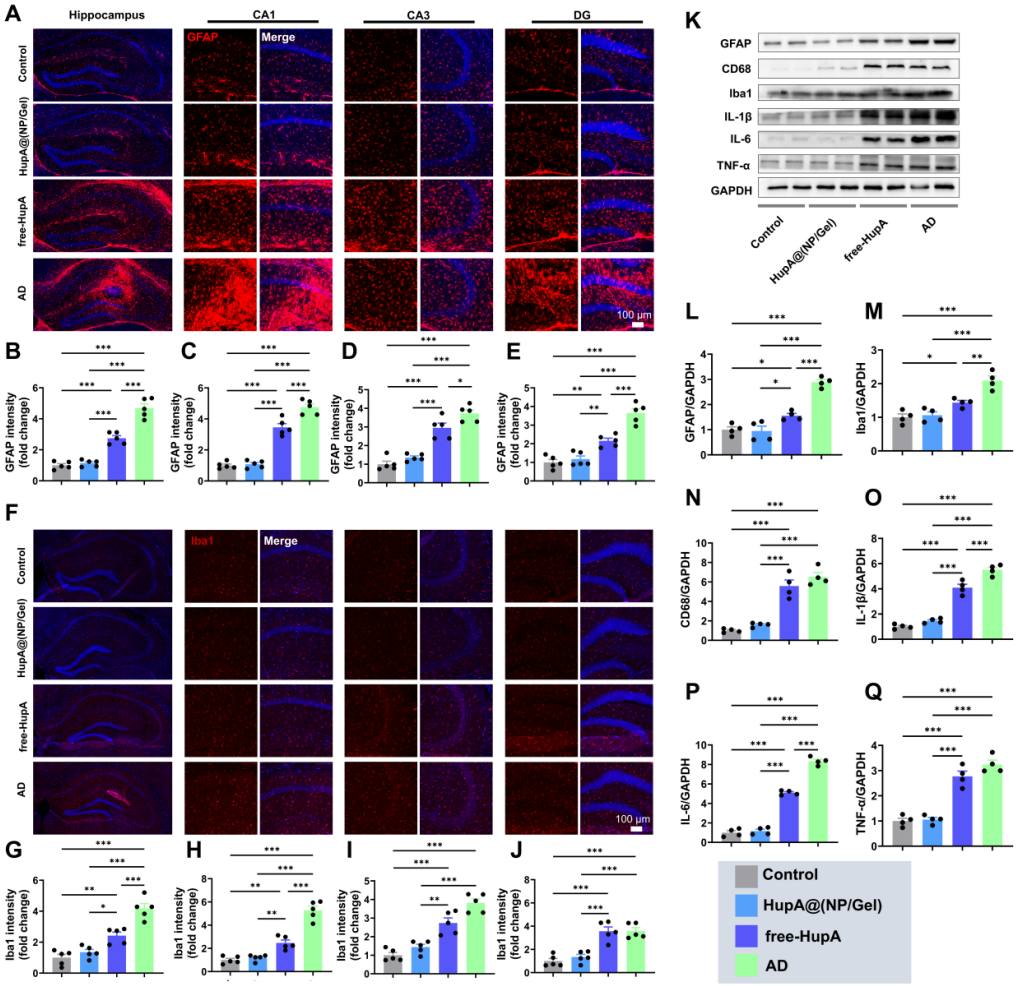

Fig. 5. HupA@(NP/Gel) treatment prevents the onset of neuroinflammation in AD mice. (**A–E**) GFAP in hippocampus: (**A**) Representative immunofluorescence images. The scale bar represents 100 μm. (**B**) Hippocampal fluorescence intensity quantification, (**C**) CA1 region intensity quantification, (**D**) CA3 region intensity quantification, (**E**) DG region intensity quantification (n = 5). (**F–J**) Iba1 in hippocampus: (**F**) Representative immunofluorescence images. The scale bar represents 100 μm. (**G**) Hippocampal fluorescence intensity quantification, (**H**) CA1 region intensity quantification, (**I**) CA3 region intensity quantification, (**J**) DG region intensity quantification (n = 5). (**K**) Representative Western blots, (**L**) GFAP relative expression quantification, (**M**) Iba1 relative expression quantification, (**N**) CD68 relative expression quantification, (**O**) IL-1β relative expression quantification, (**P**) IL-6 relative expression quantification, (**Q**) TNF-α relative expression quantification (n = 4). Data presented as mean ± SD. *$p < 0.05$, **$p < 0.01$ and ***$p < 0.001$.

HupA@(NP/Gel) treatment suppresses neuronal apoptosis, we first assessed the proportion of apoptotic neurons using Tunel staining. Results revealed significantly increased apoptotic neurons in the AD hippocampus. Notably, while a single free-HupA injection reduced apoptosis in the CA1, CA3, and DG subregions, HupA@(NP/Gel) administration demonstrated superior anti-apoptotic efficacy. Apoptotic neuron counts in the CA1 and CA3 regions of HupA@(NP/Gel)-treated mice were statistically indistinguishable from normal controls, though DG levels remained elevated ($p < 0.001$; Fig. 9**A**–**E**). We further examined key apoptosis regulators: Bcl2, Bax, and cleaved caspase 3. Immunofluorescence showed markedly enhanced cleaved caspase 3 intensity in AD mice. Free-HupA reduced cleaved caspase 3 expression, but HupA@(NP/Gel) was significantly more effective ($p < 0.001$; Fig. 9**H**–**L**). WB analysis revealed a significantly decreased Bcl-2/Bax ratio ($p < 0.01$; Fig. 9**F** and **G**) concomitantly with elevated levels of cleaved caspase-3 ($p < 0.01$; Fig. 9**M** and **N**) in AD mice. Crucially, HupA@(NP/Gel) treatment effectively reversed these alterations, increasing the Bcl-2/Bax ratio and suppressing the expression of cleaved caspase-3.

Discussion

The initial clinical manifestation of AD is progressive memory loss. As the disease advances, cognitive impairments (e.g., disorientation, attentional deficits, language disturbances) and behavioral abnormalities (e.g., anxiety,

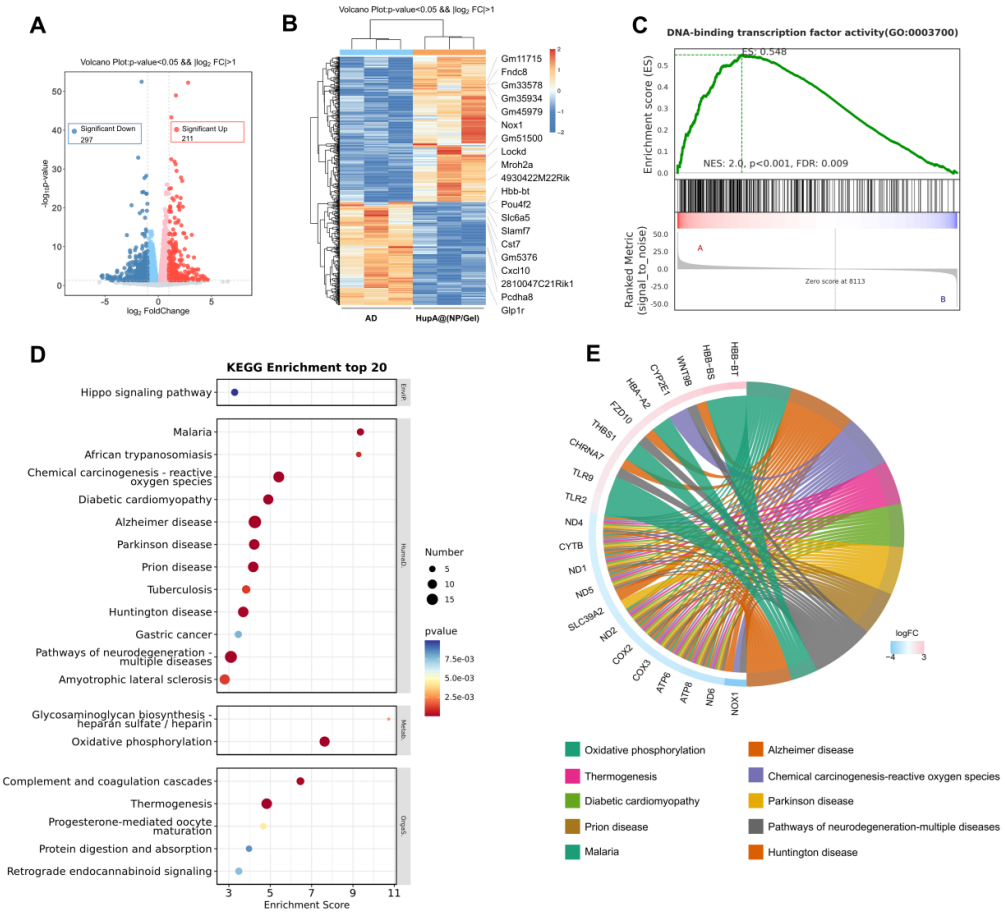

Fig. 6. Effects of HupA@(NP/Gel) treatment on the hippocampal transcriptome. (**A**) Volcano plot of differentially expressed genes (DEGs). (**B**) Cluster analysis diagram of DEGs. (**C**) Gene Set Enrichment Analysis (GSEA) plot. (**D**) Top 20 KEGG enrichment bubble plot. (**E**) Top 10 KEGG enrichment chord diagram.

delusions, depression, insomnia) emerge, significantly impairing activities of daily living [3]. AChE holds central pharmacological significance in AD treatment, primarily based on the cholinergic hypothesis [37]. As the key enzyme hydrolyzing ACh, AChEIs elevate cholinergic neurotransmission by inhibiting ACh degradation in the synaptic cleft, thereby improving memory and cognitive function [38]. Notably, AChE also possesses non-catalytic functions in AD pathology. Through its peripheral anionic site (PAS), AChE interacts with Aβ, promoting Aβ aggregation and deposition [9,39]. This suggests that AChEIs may confer dual benefits: ameliorating cholinergic deficits and potentially delaying pathological progression.

HupA, a natural alkaloid extracted from Huperzia serrata (a perennial herb of the Lycopodiaceae family), has emerged as a significant candidate for AD treatment due to its potent and selective inhibition of AChE [13,16]. Sustained HupA administration effectively improves spatial memory in AD animal models. Specifically, HupA treatment (0.25 mg/kg via oral gavage for 4 weeks) significantly reduced escape latency while increasing target quadrant entries and platform crossings in the MWM test in AD mice [40]. Similarly, in AD rat models, HupA (0.5 mg/kg/day via intraperitoneal injection for 3 weeks) improved spatial memory and NOR indices [41]. These findings collectively demonstrate HupA's efficacy in ameliorating AD-associated behavioral deficits. However, sustained therapeutic effects require continuous administration, and repeated HupA dosing poses potential safety risks and severely compromises patient compliance. Consequently, developing a novel delivery platform for controlled, sustained HupA release is critically important. PBVHx, the newest PHA, offers excellent biocompatibility and tunable biodegradability [20]. Its primary degradation product, 3HB, exhibits low tissue irritancy and has demonstrated therapeutic potential in mitigating AD pathology, positioning PBVHx as an optimal HupA carrier [16,42]. However, considering the amphiphilic nature of HupA, the encapsulation efficiency of hydrophobic polyester and hydrophilic hydrogel delivery systems is insufficient. To maximise the use of the expensive HupA, we designed a biphasic delivery platform based on PHA nanoparticles and HA gel for HupA release, theoretically achieving 100% HupA encapsulation. We prepared HupA@NPs via ultrasonic emulsifi-

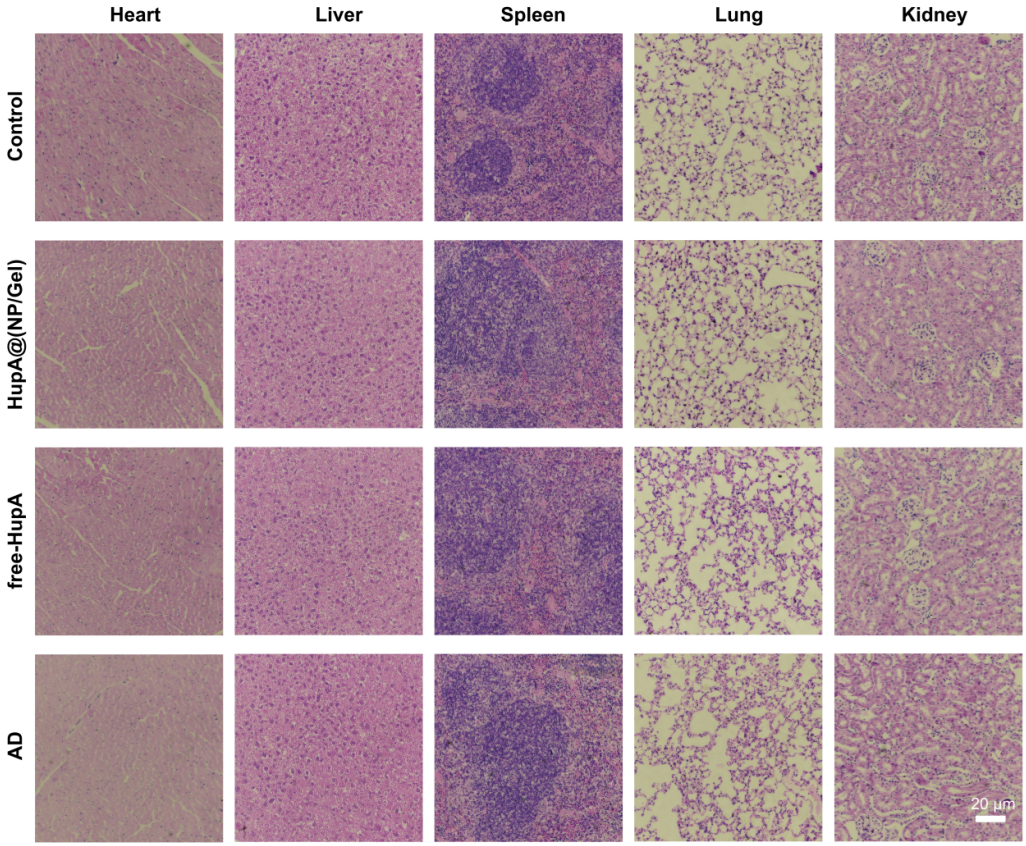

Fig. 7. H&E staining of heart, liver, spleen, lung, and kidney in each group of mice. The scale bar represents 20 μm.

cation, followed by incorporation into an HA gel matrix to achieve 100% drug loading (designated HupA@(NP/Gel)). This composite system exhibited a biphasic release profile: Phase I featured rapid HupA diffusion from the HA matrix, while Phase II provided sustained release accompanying NPs degradation. Optimization of PBVHx and HA concentrations yielded HupA@(NP/Gel) formulations sustaining HupA release for 20 days. Crucially, the gradual release kinetics significantly enhanced the system's safety profile. The 20-day sustained release duration theoretically fulfills AD therapeutic requirements, enabling single-administration, extended therapeutic coverage.

To comprehensively evaluate the behavioral impact of HupA@(NP/Gel) on AD mice, we performed multiple behavioral tests: OFT, EPM, MWM, and NOR. As shown in Fig. 3, HupA@(NP/Gel) treatment significantly reduced anxiety/depression-like behaviors, evidenced by increased frequency and duration in the open field center zone and EPM open arms. It also improved spatial memory, demonstrated by reduced escape latency and increased platform crossings in the MWM, alongside enhanced NOR indices. While a single free-HupA injection failed to ameliorate AD symptoms, sustained HupA release from HupA@(NP/Gel) effectively mediated behavioral improvements. This delivery approach demonstrated superior efficacy and safety.

HupA exhibits moderate lipophilicity (logP 2.5–3.0), enabling efficient BBB penetration via passive diffusion. It achieves therapeutic concentrations in brain tissue to exert its AChE inhibitory effects [13]. HupA intervenes in AD pathology through a multi-target mechanism: First, it potently inhibits AChE activity and reduces ACh degradation while upregulating ChAT expression to promote ACh synthesis, thereby ameliorating cholinergic deficits [43,44]. Second, HupA modulates APP processing by suppressing β-secretase activity and enhancing α-secretase (ADAM10) expression, consequently reducing Aβ_{1-42} generation [8, 18]. In this study, HupA@(NP/Gel) treatment effectively inhibited AChE activity, increased ChAT protein levels, and reduced APP, Aβ and P-Tau/Tau expression in AD mice. These effects are likely attributable to sustained HupA release from the composite system.

Enhanced cholinergic signaling significantly downregulates the expression of Iba1 (a microglial marker) and GFAP (an astrocytic marker) in the hippocampus, suppressing glial cell overactivation [45]. Wang *et al*. [46] demonstrated that HupA treatment significantly ameliorated neuroinflammation and cognitive function in 2VO rats. Post-treatment, microglia approached a resting state, astrocyte activation was reduced, and the expression of inflammatory cytokines such as IL-1β and TNF-α was significantly decreased. Studies indicate that inhibition of AChE activity elevates synaptic ACh levels. ACh binding to the α7

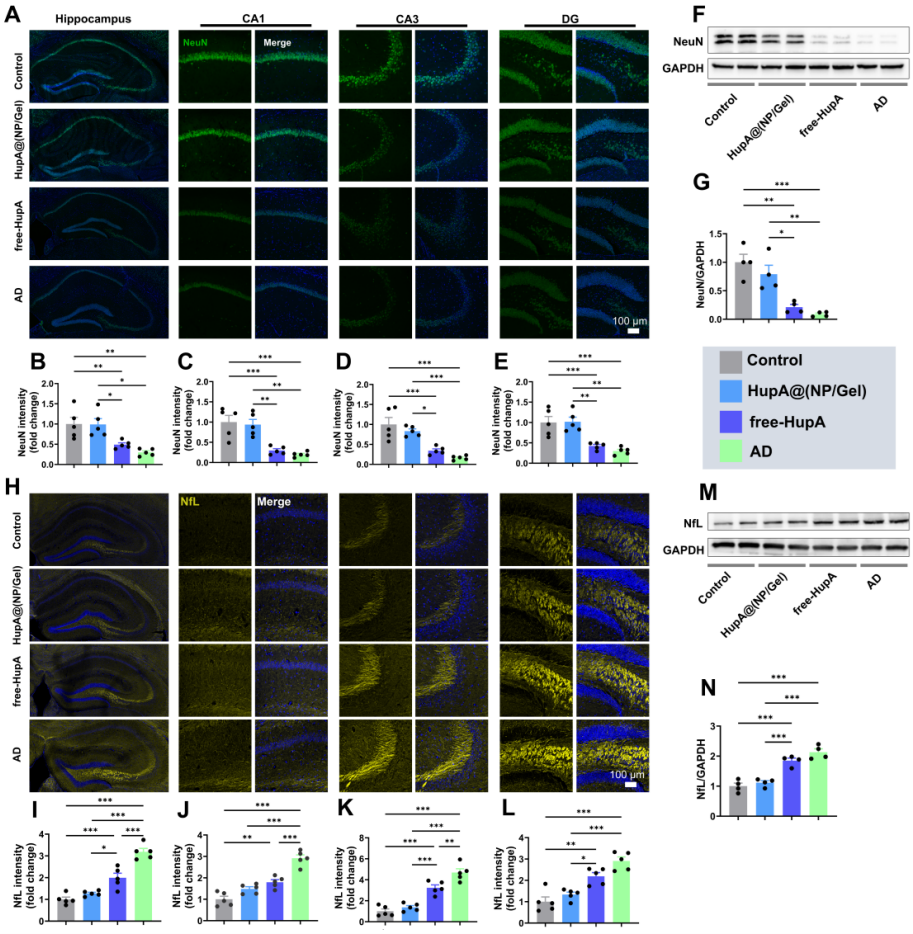

Fig. 8. HupA@(NP/Gel) treatment preserves neuronal viability and axonal integrity in AD mice. (**A–E**) NeuN in hippocampus: (**A**) Representative immunofluorescence images. The scale bar represents 100 μm. (**B**) Hippocampal fluorescence intensity quantification, (**C**) CA1 region intensity quantification, (**D**) CA3 region intensity quantification, (**E**) DG region intensity quantification (n = 5). (**F**) Western blot bands for NeuN protein. (**G**) Relative expression level of NeuN protein (n = 4). (**H–L**) NfL in hippocampus: (**H**) Representative immunofluorescence images. The scale bar represents 100 μm. (**I**) Hippocampal fluorescence intensity quantification, (**J**) CA1 region intensity quantification, (**K**) CA3 region intensity quantification, (**L**) DG region intensity quantification (n = 5). (**M**) Western blot bands for NfL protein. (**N**) Relative expression level of NfL protein (n = 4). Data presented as mean ± SD. *$p < 0.05$, **$p < 0.01$ and ***$p < 0.001$.

nicotinic acetylcholine receptor (α7nAChR) on glial cells activates the downstream JAK2/STAT3 pathway and suppresses NF-κB nuclear translocation, significantly reducing hippocampal NF-κB p65 phosphorylation levels and further diminishing pro-inflammatory cytokine expression [46,47]. α7nAChR activation also promotes microglial polarization towards the anti-inflammatory M2 phenotype [48]. Activated M2 microglia clear Aβ via TREM2-mediated phagocytosis, thereby reducing Aβ-driven inflammatory feedback [49]. This study employed both immunofluorescence and WB analyses to validate the expression of Iba1, CD68, and GFAP. Results showed that AD significantly upregulated these proteins in the hippocampus. While free-HupA provided some prevention against abnormal microglial and astrocytic activation, its efficacy was inferior to that of the HupA@(NP/Gel) treatment group. The sustained release of HupA from HupA@(NP/Gel) was demonstrated to be crucial for maintaining glial cell homeostasis. Furthermore, assessment of IL-1β, TNF-α, and IL-6 protein expression confirmed that HupA@(NP/Gel) treatment significantly reduced hippocampal inflammation levels in AD mice, as anticipated.

Mitochondrial dysfunction in glial cells plays a critical role in the pathogenesis of AD. Aβ deposition disrupts mitochondrial function through multiple pathways [50]. On one hand, Aβ induces excessive mitochondrial fragmentation by activating the fission protein Drp1 and inhibiting fusion proteins (e.g., OPA1, Mfn2), thereby disrupting mitochondrial network integrity [51]. On the other hand, Aβ directly interacts with mitochondrial membranes, impairing the activity of electron transport chain (ETC) complexes (particularly complex IV), leading to excessive ROS generation and suppression of antioxidant enzyme activity (e.g., SOD2), which exacerbates oxidative damage

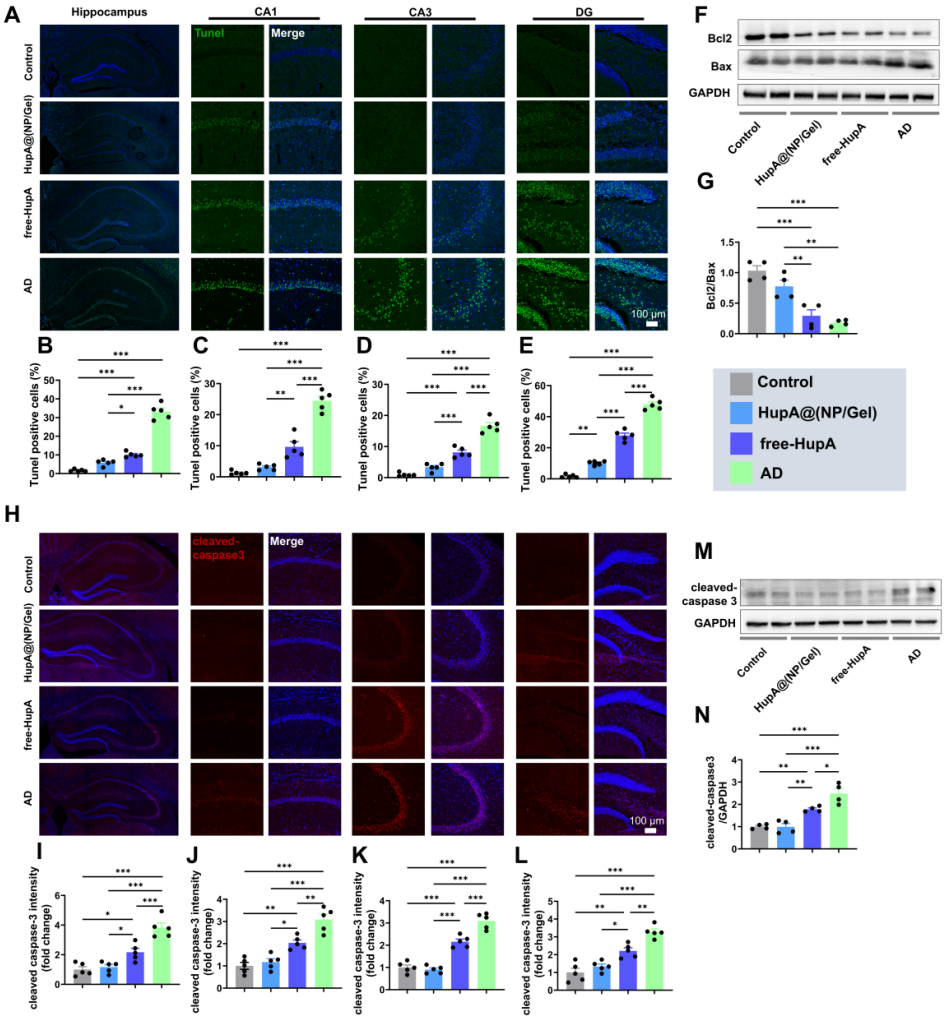

Fig. 9. HupA@(NP/Gel) treatment prevents neuronal apoptosis. (**A–E**) Tunel-positive cells in hippocampus: (**A**) Representative immunofluorescence images. The scale bar represents 100 μm. (**B**) Hippocampal fluorescence intensity quantification, (**C**) CA1 region intensity quantification, (**D**) CA3 region intensity quantification, (**E**) DG region intensity quantification (n = 5). (**F**) Western blot bands for Bcl2 and Bax proteins. (**G**) Bcl2/Bax ratio (n = 4). (**H–L**) cleaved-caspase 3 in hippocampus: (**H**) Representative immunofluorescence images. The scale bar represents 100 μm. (**I**) Hippocampal fluorescence intensity quantification, (**J**) CA1 region intensity quantification, (**K**) CA3 region intensity quantification, (**L**) DG region intensity quantification (n = 5). (**M**) Western blot bands for cleaved-caspase 3 protein. (**N**) Relative expression level of cleaved-caspase 3 protein (n = 4). Data presented as mean ± SD. *$p < 0.05$, **$p < 0.01$ and ***$p < 0.001$.

[52,53]. Transcriptomic analysis in this study confirmed that AD pathology is mediated by the synergistic effects of mitochondrial dysfunction and ROS accumulation. However, HupA@(NP/Gel) treatment effectively prevented mitochondrial dysfunction in AD mice. HupA ameliorates mitochondrial impairment; treatment restores ATP production and significantly suppresses the expression of the inner mitochondrial membrane protein cytochrome c (Cyt c) in AD mice [18].

Mitochondrial dysfunction in AD pathogenesis acts not only as a driver of energy metabolism collapse but also as a central trigger for neuronal apoptosis. Aβ accumulation within mitochondria induces aberrant mitochondrial permeability transition pore (mPTP) opening. This disrupts mitochondrial membrane potential ($\Delta\Psi$m), leading to the release of Cyt c and apoptosis-inducing factor (AIF), thereby activating the caspase 9/caspase 3 cascade [16,24]. Concurrently, excessive ROS generated by impaired mitochondrial respiratory chain function activates the JNK signaling pathway. This further phosphorylates Bcl2, promoting its dissociation from Bax and amplifying the apoptotic signal [50,54]. The anti-apoptotic effect of HupA is well-established. In Aβ-treated neurons, HupA prevents the phosphorylation-induced inactivation of Bcl2 while downregulating mitochondrial translocation of Bax, thereby maintaining the anti-apoptotic/pro-apoptotic protein ratio [55]. This study revealed a significant increase in apoptotic neuronal cells and cleaved cas-

pase 3-positive cells within the hippocampus of AD mice. HupA@(NP/Gel) treatment effectively prevented neuronal apoptosis, a protective effect likely closely associated with modulation of the Bcl2/Bax apoptotic pathway. NeuN, a neuron-specific nuclear protein widely used as a marker for mature neurons, exhibits expression levels closely correlated with neuronal survival and functional integrity [56]. AD is characterized by significant neuronal loss in vulnerable brain regions such as the hippocampus and entorhinal cortex. In AD transgenic mice, reduced the NeuN expression demonstrates a close association with Aβ plaque deposition [57]. Our assessment of NeuN protein confirmed neuronal loss during AD progression. Crucially, sustained HupA release from HupA@(NP/Gel) treatment reversed this neuronal loss, an effect potentially mediated by the amelioration of mitochondrial function.

NfL, a component of neurofilament proteins predominantly located in neuronal axons, plays a critical role in axonal and dendritic branching and growth. Elevated NfL release into CSF or blood reflects axonal damage or neuronal loss, serving as an important biomarker for the clinical diagnosis of neurodegenerative diseases such as AD [58]. Clinical studies confirm that NfL levels increase during the early stages of AD, indicating axonal damage precedes the onset of clinical symptoms [58,59]. Elevated CSF NfL levels are observed even in the asymptomatic phase of AD mice, with levels closely correlated with the progression of brain damage and the extent of neuronal loss [36]. Aβ oligomers bind to neuronal membrane receptors (e.g., mGluR5), activating downstream calcium signaling pathways (e.g., IP3R-Ca^{2+}). This leads to intra-axonal calcium overload; the resulting disruption of calcium homeostasis destabilizes neurofilament proteins, promoting NfL release [60,61]. This study found increased hippocampal NfL protein expression during AD progression. Crucially, HupA@(NP/Gel) treatment effectively prevented abnormal NfL accumulation in axonal proximal regions. This protective effect is closely associated with the sustained release of HupA from HupA@(NP/Gel), which prevents Aβ deposition, reduces brain ROS levels, and protects mitochondrial function.

However, it is important to acknowledge that HupA@(NP/Gel) exhibits inherent limitations in the treatment of AD. Firstly, the relatively high cost of PHA results in elevated production expenses for HupA@(NP/Gel), which poses challenges to its clinical translation and application. Secondly, further evaluations of the safety profile and long-term stability of HupA@(NP/Gel) are necessary, including assessments of its cytotoxicity, hemocompatibility, *in vivo* distribution, and pharmacokinetic properties. Thirdly, this study lacks direct experimental evidence, such as *in vivo* imaging, to demonstrate that the HupA@(NP/Gel) system can penetrate the BBB. Fourthly, the experimental design was confined to male C57BL/6 mice, and female mice were not included in this investigation. These limitations highlight critical areas that require in-depth and comprehensive resolution in subsequent research.

Conclusions

In summary, we have developed a novel biphasic delivery platform, HupA@ (NP/Gel), as an effective carrier for HupA, which achieves 100% HupA loading and enables sustained, controlled release of HupA. The biphasic release characteristics of the platform allow for sustained release of HupA for over 20 days, making it effective for the management of AD. *In vivo*, A single injection of HupA@(NP/Gel) significantly improved spatial memory, effectively reduced AChE activity, APP levels, and Aβ deposition. Furthermore, it suppressed aberrant activation of microglia and astrocytes, decreasing pro-inflammatory cytokine release. Transcriptome analysis indicated that HupA@(NP/Gel) treatment notably enhanced mitochondrial function, reduced neuronal loss, and preserved axonal integrity. Consequently, HupA@(NP/Gel) represents a highly promising platform for safe and effective AD treatment, offering new insights for biomaterial design targeting neurodegenerative disorders.

List of Abbreviations

HupA, huperzine A; AD, Alzheimer's disease; HA, hyaluronic acid; Aβ, β-amyloid; Ach, acetylcholine; mAChRs, metabotropic muscarinic receptors; nAChRs, ionotropic nicotinic receptors; APP, amyloid precursor protein; AChE, acetylcholinesterase; BBB, blood-brain barrier; CSF, cerebrospinal fluid; AChEIs, AChE inhibitors; NP, nanoparticle; PHA, Polyhydroxyalkanoate; 3HB, 3-hydroxybutyrate; 3HV, 3-hydroxyvalerate; 3HHx, 3-hydroxyhexanoate; EE, encapsulation efficiency; DCM, Dichloromethane; PVA, polyvinyl alcohol; RT, room temperature; TEM, transmission electron microscopy; OFT, open field test; EPM, elevated plus maze; NOR, novel object recognition; MWM, Morris water maze; H&E, hematoxylin and eosin; DEGs, differentially expressed genes; GSEA, gene set enrichment analysis; NfL, neurofilament light chain. ETC, electron transport chain; Cyt c, cytochrome c.

Availability of Data and Materials

The dataset supporting this study is available from the corresponding author upon reasonable request.

Author Contributions

JFW, YWZ and YL conducted bioinformatic analysis, wrote the manuscript, and were responsible for language revisions. YY, YDT, YGT, DFC and KZL helped with some of the experiments. DXW designed the study. All authors reviewed and approved the final manuscript. Each author takes ultimate responsibility for ensuring the integrity of the

work, committing to the thorough investigation and resolution of any concerns regarding its accuracy.

Ethics Approval and Consent to Participate

All animal studies, conducted in accordance with national guidelines and approved by the Zigong Mental Health Center Ethics Committee (ZPRC-20240523), were designed to minimize pain and distress.

Acknowledgments

We gratefully acknowledge the instrumental contributions of the Animal Research Center at the Zigong Institute of Brain Science to the entire research process.

Funding

This work was supported by grants from the National Natural Science Foundation of China (31900950); National Key Research and Development Program of China (2022YFC2009900); Natural Science Basic Research Plan in Shaanxi Province of China (2024JC-YBMS-706), Key Science and Technology Plan Projects in Zigong (2022ZCNKY12, 2023-NKY-01-02, 2023-NKY-02-13, 2024-NKY-02-09, 2024-NKY-01-01, 2025-NKY-01-03 and 2023-NKY-02-14); Key Science and Technology Plan of Zigong City (Collaborative Innovation Category of Zigong Integrated Traditional Chinese and Western Medicine Research Institute) (2025ZXY0101, 2025ZXY0206 and 2025ZXY0322); Zigong Key Science and Technology Program — Zigong Academy for Medical Big Data and Artificial Intelligence Joint Project (2023-YGY-1-02 and 2024-YGY-02-04); Health Commission of Sichuan Province Medical Science and Technology Program (24WSXT106) and Scientific Research Project of Zigong Health Commission (22yb001 and 24zd008).

Conflict of Interest

The authors declare no competing financial interests or relevant personal relationships.

References

[1] Estimation of the global prevalence of dementia in 2019 and forecasted prevalence in 2050: an analysis for the Global Burden of Disease Study 2019. Lancet Public Health. 2022; 7: e105–e125. https://doi.org/10.1016/s2468-2667(21)00249-8.

[2] Feng Q, Zhang X, Zhang N, Gu H, Wang N, Chen J, *et al*. The dissolution, reassembly and further clearance of amyloid-β fibrils by tailor-designed dissociable nanosystem for Alzheimer's disease therapy. Exploration (Beijing, China). 2024; 4: 20230048. https://doi.org/10.1002/exp.20230048.

[3] Lopez-Lee C, Torres ERS, Carling G, Gan L. Mechanisms of sex differences in Alzheimer's disease. Neuron. 2024; 112: 1208–1221. https://doi.org/10.1016/j.neuron.2024.01.024.

[4] Zheng Q, Wang X. Alzheimer's disease: insights into pathology, molecular mechanisms, and therapy. Protein Cell. 2025; 16: 83–120. https://doi.org/10.1093/procel/pwae026.

[5] Richter N, Breidenbach L, Schmieschek MH, Heiss WD, Fink GR, Onur OA. Alzheimer-typical temporo-parietal atrophy and hypoperfusion are associated with a more significant cholinergic impairment in amnestic neurodegenerative syndromes. Journal of Alzheimer's disease: JAD. 2025; 104: 1290–1300. https://doi.org/10.1177/13872877251324080.

[6] Xie Z, Li L, Hou W, Fan Z, Zeng L, He L, *et al*. Critical role of Oas1g and STAT1 pathways in neuroinflammation: insights for Alzheimer's disease therapeutics. J Transl Med. 2025; 23: 182. https://doi.org/10.1186/s12967-025-06112-2.

[7] Prajapati SK, Pathak A, Samaiya PK. Alzheimer's disease: from early pathogenesis to novel therapeutic approaches. Metabolic Brain Disesae. 2024; 39: 1231–1254. https://doi.org/10.1007/s11011-024-01389-6.

[8] Khezri MR, Mohebalizadeh M, Ghasemnejad-Berenji M. Therapeutic potential of ADAM10 modulation in Alzheimer's disease: a review of the current evidence. Cell communication and signaling: CCS. 2023; 21: 60. https://doi.org/10.1186/s12964-023-01072-w.

[9] Ghasemi A, Qaffaripour Z, Tourani M, Saleki K, Rahmani-Kukia N, Khatami SH, *et al*. The relationship between long non-coding RNAs and Wnt/β-catenin signaling pathway in the pathogenesis of Alzheimer's disease. Experimental neurology. 2023; 366: 114434. https://doi.org/10.1016/j.expneurol.2023.114434.

[10] Parnetti L, Chiasserini D, Andreasson U, Ohlson M, Hüls C, Zetterberg H, *et al*. Changes in CSF acetyl- and butyrylcholinesterase activity after long-term treatment with AChE inhibitors in Alzheimer's disease. Acta neurologica Scandinavica. 2011; 124: 122–129. https://doi.org/10.1111/j.1600-0404.2010.01435.x.

[11] Battle CE, Abdul-Rahim AH, Shenkin SD, Hewitt J, Quinn TJ. Cholinesterase inhibitors for vascular dementia and other vascular cognitive impairments: a network meta-analysis. The Cochrane database of systematic reviews. 2021; 2: CD013306. https://doi.org/10.1002/14651858.CD013306.pub2.

[12] Marucci G, Buccioni M, Ben DD, Lambertucci C, Volpini R, Amenta F. Efficacy of acetylcholinesterase inhibitors in Alzheimer's disease. Neuropharmacology. 2021; 190: 108352. https://doi.org/10.1016/j.neuropharm.2020.108352.

[13] Yan YP, Chen JY, Lu JH. Disease-Modifying Activity of Huperzine A on Alzheimer's Disease: Evidence from Preclinical Studies on Rodent Models. International journal of molecular sciences. 2022; 23: 15238. https://doi.org/10.3390/ijms232315238.

[14] Nett RS, Dho Y, Low YY, Sattely ES. A metabolic regulon reveals early and late acting enzymes in neuroactive Lycopodium alkaloid biosynthesis. Proceedings of the National Academy of Sciences of the United States of America. 2021; 118: e2102949118. https://doi.org/10.1073/pnas.2102949118.

[15] Jiang H, Luo X, Bai D. Progress in clinical, pharmacological, chemical and structural biological studies of huperzine A: a drug of traditional chinese medicine origin for the treatment of Alzheimer's disease. Current medicinal chemistry. 2003; 10: 2231–2252. https://doi.org/10.2174/0929867033456747.

[16] Wei DX, Cai D, Tan Y, Liu K, Dao JW, Li X, *et al*. Poly(3-hydroxybutyrate-co-3-hydroxyvalerate-co-3-hydroxyhexanoate)-based microspheres as a sustained platform for Huperzine A delivery for alzheimer's disease therapy. International journal of biological macromolecules. 2024; 282: 136582. https://doi.org/10.1016/j.ijbiomac.2024.136582.

[17] Zhang RH, Wang C, Shi T, Chen XJ, Xu JF, Shi M, *et al*. Pharmacokinetics of HupA-PLGA-NPs of different sizes in the mouse blood and brain determined by LC-MS/MS. European review for medical and pharmacological sciences. 2022; 26: 1183–1195. https://doi.org/10.26355/eurrev_202202_28111.

[18] Xiao X, Chen Q, Zhu X, Wang Y. ABAD/17β-HSD10 reduction contributes to the protective mechanism of huperzine a on the cerebral mitochondrial function in APP/PS1 mice. Neurobiol of Aging. 2019; 81: 77–87. https://doi.org/10.1016/j.neurobiolaging.2019.05.016.

[19] Ding YW, Li Y, Zhang ZW, Dao JW, Wei DX. Hy-

drogel forming microneedles loaded with VEGF and Ritlecitinib/polyhydroxyalkanoates nanoparticles for mini-invasive androgenetic alopecia treatment. Bioactive materials. 2024; 38: 95–108. https://doi.org/10.1016/j.bioactmat.2024.04.020.

[20] Ren ZW, Wang ZY, Ding YW, Dao JW, Li HR, Ma X, *et al*. Polyhydroxyalkanoates: the natural biopolyester for future medical innovations. Biomaterials science. 2023; 11: 6013–6034. https://doi.org/10.1039/d3bm01043k.

[21] Wei DX, Chen Z. Current situation and challenge of exogenous 3-hydroxybutyrate derived from polyhydroxyalkanoates for elderly health: A review. International journal of biological macromolecules. 2025; 285: 138328. https://doi.org/10.1016/j.ijbiomac.2024.138328.

[22] Wang BL, Wu JF, Xiao D, Wu B, Wei DX. 3-hydroxybutyrate in the brain: Biosynthesis, function, and disease therapy. Brain-X. 2023; 1. https://doi.org/10.1002/brx2.6.

[23] Biswas B, Misra TK, Ray D, Majumder T, Bandyopadhyay TK, Bhowmick TK. Current therapeutic delivery approaches using nanocarriers for the treatment of tuberculosis disease. International journal of pharmaceutics. 2023; 640: 123018. https://doi.org/10.1016/j.ijpharm.2023.123018.

[24] Huang XY, Qi ZD, Dao JW, Wei DX. Current situation and challenges of polyhydroxyalkanoates-derived nanocarriers for cancer therapy. Smart Materials in Medicine. 2024; 5: 529–541. https://doi.org/https://doi.org/10.1016/j.smaim.2024.10.004.

[25] Roghani AK, Garcia RI, Roghani A, Reddy A, Khemka S, Reddy RP, *et al*. Treating Alzheimer's disease using nanoparticle-mediated drug delivery strategies/systems. Ageing research reviews. 2024; 97: 102291. https://doi.org/10.1016/j.arr.2024.102291.

[26] Feng Y, Zhang Z, Tang W, Dai Y. Gel/hydrogel-based in situ biomaterial platforms for cancer postoperative treatment and recovery. Exploration (Beijing, China). 2023; 3: 20220173. https://doi.org/10.1002/exp.20220173.

[27] J.K.Venkatesan, W.Liu, H.Madry, M.Cucchiarini. Alginate hydrogel-guided rAAV-mediated FGF-2 and TGF-β delivery and overexpression stimulates the biological activities of human meniscal fibrochondrocytes for meniscus repair. European Cells and Materials. 2024; 47: 1–14. https://doi.org/10.22203/eCM.v047a01.

[28] Graça MFP, Miguel SP, Cabral CSD, Correia IJ. Hyaluronic acid-Based wound dressings: A review. Carbohydrate polymers. 2020; 241: 116364. https://doi.org/10.1016/j.carbpol.2020.116364.

[29] Carton F, Malatesta M. Nanotechnological Research for Regenerative Medicine: The Role of Hyaluronic Acid. International journal of molecular sciences. 2024; 25: 3975. https://doi.org/10.3390/ijms25073975.

[30] Wei H, Gao Z, Zheng L, Zhang C, Liu Z, Yang Y, *et al*. Protective Effects of Fucoidan on Aβ25-35 and d-Gal-Induced Neurotoxicity in PC12 Cells and d-Gal-Induced Cognitive Dysfunction in Mice. Marine Drugs. 2017; 15: 77. https://doi.org/10.3390/md15030077.

[31] Wang H, Zhou L, Zheng Q, Song Y, Huang W, Yang L, *et al*. Kai-xin-san improves cognitive impairment in D-gal and Aβ(25-35) induced ad rats by regulating gut microbiota and reducing neuronal damage. Journal of ethnopharmacology. 2024; 329: 118161. https://doi.org/10.1016/j.jep.2024.118161.

[32] Wu J, Liu Y, Wang B, Wang Y, Liu B, Tan Y, *et al*. A potential strategy for improving offspring behavior in maternal immune activation: Amantadine-mediated suppression of neuroinflammation. Animal models and experimental medicine. 2025; 8: 1836–1850. https://doi.org/10.1002/ame2.70059.

[33] Wu J, Wang B, Tan Y, Liu K, Liu X, Liu S, *et al*. Ligustilide Ameliorates Traumatic Brain Injury in Aged Mice by Attenuating Microglia-Mediated Neuroinflammation. Neurochemical research. 2025; 50: 309. https://doi.org/10.1007/s11064-025-04560-2.

[34] Tsering W, de la Rosa A, Ruan IY, Philips JL, Bathe T, Villareal JA, *et al*. Preferential clustering of microglia and astrocytes around neuritic plaques during progression of Alzheimer's disease neuropathological changes. Journal of neurochemistry. 2025; 169: e16275. https://doi.org/10.1111/jnc.16275.

[35] Ashleigh T, Swerdlow RH, Beal MF. The role of mitochondrial dysfunction in Alzheimer's disease pathogenesis. Alzheimer's & Dementia. 2023; 19: 333–342. https://doi.org/10.1002/alz.12683.

[36] Fuloria NK, Sekar M, Porwal O, Ansari MT, Biswas A, Narain K, *et al*. Neurofilament light chain in Alzheimer's disease. Clinica chimica acta; international journal of clinical chemistry. 2026; 578: 120580. https://doi.org/10.1016/j.cca.2025.120580.

[37] Walczak-Nowicka Ł J, Herbet M. Acetylcholinesterase Inhibitors in the Treatment of Neurodegenerative Diseases and the Role of Acetylcholinesterase in their Pathogenesis. International journal of molecular sciences. 2021; 22: 9290. https://doi.org/10.3390/ijms22179290.

[38] Akıncıoğlu H, Gülçin İ. Potent Acetylcholinesterase Inhibitors: Potential Drugs for Alzheimer's Disease. Mini reviews in medicinal chemistry. 2020; 20: 703–715. https://doi.org/10.2174/1389557520666200103100521.

[39] Singh A, Verma A, Bhardwaj B, Saraf P, Kumar H, Jain N, *et al*. Structure-Guided Design, Synthesis, and Biological Evaluation of Peripheral Anionic Site Selective and Brain Permeable Novel Oxadiazole-Piperazine Conjugates against Alzheimer's Disease with Antioxidant Potential. ACS Omega. 2024; 9: 18169–18182. https://doi.org/10.1021/acsomega.3c10276.

[40] Nie H, Wang Z, Zhao W, Lu J, Zhang C, Lok K, *et al*. New nicotinic analogue ZY-1 enhances cognitive functions in a transgenic mice model of Alzheimer's disease. Neuroscience letters. 2013; 537: 29–34. https://doi.org/10.1016/j.neulet.2013.01.001.

[41] Rispoli V, Ragusa S, Nisticò R, Marra R, Russo E, Leo A, *et al*. Huperzine a restores cortico-hippocampal functional connectivity after bilateral AMPA lesion of the nucleus basalis of meynert. Journal of Alzheimer's disease: JAD. 2013; 35: 833–846. https://doi.org/10.3233/jad-130278.

[42] Shippy DC, Wilhelm C, Viharkumar PA, Raife TJ, Ulland TK. β-Hydroxybutyrate inhibits inflammasome activation to attenuate Alzheimer's disease pathology. Journal of neuroinflammation. 2020; 17: 280. https://doi.org/10.1186/s12974-020-01948-5.

[43] De La Garza R 2nd, Verrico CD, Newton TF, Mahoney JJ 3rd, Thompson-Lake DG. Safety and Preliminary Efficacy of the Acetylcholinesterase Inhibitor Huperzine A as a Treatment for Cocaine Use Disorder. The international journal of neuropsychopharmacology. 2015; 19: pyv098. https://doi.org/10.1093/ijnp/pyv098.

[44] Cheng DH, Tang XC. Comparative studies of huperzine A, E2020, and tacrine on behavior and cholinesterase activities. Pharmacology, biochemistry, and behavior. 1998; 60: 377–386. https://doi.org/10.1016/s0091-3057(97)00601-1.

[45] Younis RL, El-Gohary RM, Ghalwash AA, Hegab II, Ghabrial MM, Aboshanady AM, *et al*. Luteolin Mitigates D-Galactose-Induced Brain Ageing in Rats: SIRT1-Mediated Neuroprotection. Neurochemical research. 2024; 49: 2803–2820. https://doi.org/10.1007/s11064-024-04203-y.

[46] Wang J, Zhang HY, Tang XC. Huperzine a improves chronic inflammation and cognitive decline in rats with cerebral hypoperfusion. Journal of neuroscience research. 2010; 88: 807–815. https://doi.org/10.1002/jnr.22237.

[47] Chen Y, Zhang Y, Wang J, Li S, Wang Y, Zhang Z, *et al*. Anti-neuroinflammation effects of transcutaneous auricular vagus nerve stimulation against depression-like behaviors via hypothalamic α7nAchR/JAK2/STAT3/NF-κB pathway in rats exposed to chronic unpredictable mild stress. CNS neuroscience & therapeutics. 2023; 29: 2634–2644. https://doi.org/10.1111/cns.14207.

[48] Niu XH, Liu RH, Lv X, He RL, Lv FZ, Wu SJ, *et al*. Activating α7nAChR helps post-myocardial infarction healing by regulating macrophage polarization via the STAT3 signaling pathway. Inflamm Res. 2023; 72: 879–892. https://doi.org/10.1007/s00011-023-01714-2.

[49] van Olst L, Simonton B, Edwards AJ, Forsyth AV, Boles J, Jamshidi P, *et al*. Microglial mechanisms drive amyloid-β clearance in immunized patients with Alzheimer's disease. Nature medicine. 2025; 31: 1604–1616. https://doi.org/10.1038/s41591-025-03574-1.

[50] Li Y, Xia X, Wang Y, Zheng JC. Mitochondrial dysfunction in microglia: a novel perspective for pathogenesis of Alzheimer's disease. Journal of neuroinflammation. 2022; 19: 248. https://doi.org/10.1186/s12974-022-02613-9.

[51] Kandimalla R, Manczak M, Pradeepkiran JA, Morton H, Reddy PH. A partial reduction of Drp1 improves cognitive behavior and enhances mitophagy, autophagy and dendritic spines in a transgenic Tau mouse model of Alzheimer disease. Human molecular genetics. 2022; 31: 1788–1805. https://doi.org/10.1093/hmg/ddab360.

[52] Nabi SU, Khan A, Siddiqui EM, Rehman MU, Alshahrani S, Arafah A, *et al*. Mechanisms of Mitochondrial Malfunction in Alzheimer's Disease: New Therapeutic Hope. Oxidative medicine and cellular longevity. 2022; 2022: 4759963. https://doi.org/10.1155/2022/4759963.

[53] Gao JM, Zhang X, Shu GT, Chen NN, Zhang JY, Xu F, *et al*. Trilobatin rescues cognitive impairment of Alzheimer's disease by targeting HMGB1 through mediating SIRT3/SOD2 signaling pathway. Acta pharmacologica Sinica. 2022; 43: 2482–2494. https://doi.org/10.1038/s41401-022-00888-5.

[54] Shi Z, Zhang K, Zhou H, Jiang L, Xie B, Wang R, *et al*. Increased miR-34c mediates synaptic deficits by targeting synaptotagmin 1 through ROS-JNK-p53 pathway in Alzheimer's Disease. Aging Cell. 2020; 19: e13125. https://doi.org/10.1111/acel.13125.

[55] Shukla M, Wongchitrat P, Govitrapong P. A Synopsis of Multitarget Potential Therapeutic Effects of Huperzine A in Diverse Pathologies-Emphasis on Alzheimer's Disease Pathogenesis. Neurochemical research. 2022; 47: 1166–1182. https://doi.org/10.1007/s11064-022-03530-2.

[56] Gómez-Isla T, Hollister R, West H, Mui S, Growdon JH, Petersen RC, *et al*. Neuronal loss correlates with but exceeds neurofibrillary tangles in Alzheimer's disease. Annals of neurology. 1997; 41: 17–24. https://doi.org/10.1002/ana.410410106.

[57] Zhang P, Liu Y, Jin X, Hu Z, Yang J, Lu H, *et al*. Alzheimer's disease-like pathology induced by Porphyromonas gingivalis in middle-aged mice is mediated by NLRP3 inflammasome via the microbiota-gut-brain axis. Journal of Alzheimer's disease: JAD. 2025; 103: 487–505. https://doi.org/10.1177/13872877241302498.

[58] Teunissen CE, Verberk IMW, Thijssen EH, Vermunt L, Hansson O, Zetterberg H, *et al*. Blood-based biomarkers for Alzheimer's disease: towards clinical implementation. The Lancet. Neurology. 2022; 21: 66–77. https://doi.org/10.1016/s1474-4422(21)00361-6.

[59] Cai H, Pang Y, Fu X, Ren Z, Jia L. Plasma biomarkers predict Alzheimer's disease before clinical onset in Chinese cohorts. Nature communications. 2023; 14: 6747. https://doi.org/10.1038/s41467-023-42596-6.

[60] He L, de Souto Barreto P, Aggarwal G, Nguyen AD, Morley JE, Li Y, *et al*. Plasma Aβ and neurofilament light chain are associated with cognitive and physical function decline in non-dementia older adults. Alzheimer's research & therapy. 2020; 12: 128. https://doi.org/10.1186/s13195-020-00697-0.

[61] Sanjay, Sood R, Jaiswal V, Kang SU, Park M, Lee HJ. Nobiletin regulates intracellular Ca^{2+} levels via IP_3 R and ameliorates neuroinflammation in Aβ42-induced astrocytes. Redox biology. 2024; 73: 103197. https://doi.org/10.1016/j.redox.2024.103197.

Editor's note: The Scientific Editor responsible for this paper was Yang Liu.

Received: 24th December 2025; **Accepted**: 6th January 2026; **Published**: 29th May 2026